GSA Data Repository 2016234

Paleomagnetic constraints on the Mesozoic drift of the Lhasa terrane (Tibet) from Gondwana to Eurasia

Zhenyu Li [a, d], Lin Ding [a, b*], Peter C. Lippert [c], Peiping Song [a], Yahui Yue [a], and Douwe J.J. van Hinsbergen [d]

a. Key Laboratory of Continental Collision and Plateau Uplift (LCPU), Institute of Tibetan Plateau Research, Chinese Academy of Sciences (ITPCAS), Beijing 100101, China;
b. Center for Excellence in Tibetan Plateau Earth Sciences, Chinese Academy of Sciences Beijing 100101, China;
c. Department of Geology and Geophysics, University of Utah, Salt Lake City, Utah, UT 84112-9057, USA;
d. Department of Earth Sciences, University of Utrecht, Heidelberglaan 4, 3584 CD Utrecht, the Netherlands.
* Corresponding Author: Prof. Dr. Lin Ding, E-mail: dinglin@itpcas.ac.cn, Fax: +86 10 8409 7049.

A1. Field Mapping and Sampling

Field mapping and sample-collecting campaigns were completed during two successive field seasons during the summer of 2011 and the autumn of 2012. Our work focused on two sampling locations: one within Sangri County (29°17.716'N, 92°02.852'E) and the other distributed around Sangye Town along the northern bank of the Indus-Yarlung-Zangbo river (29°18.005'N, 91°34.241'E) (yellow dots in Figure DR1).

Two bulk samples (red-colored dots in Figure DR1) for zircon U-Pb dating were collected from freshly exposed basaltic andesite outcrops at the Sangri County location. Sample 2011TS06-7 was collected from the upper lavas of the section, whereas sample 2011TS06-11 was collected from the lower lavas of the same section.

Paleomagnetic sampling sites consist of basaltic andesite and andesite (yellow dots in Figure DR1) and were selected based on field evidence for distinct lava flows, such as vesicle distributions, oxidation surfaces, scoria, and crystal size distributions. Eight to ten independently oriented paleomagnetic samples were drilled across 1-3 meters of lateral section and the height of each sampling site using a portable gasoline-powered drill (Figure DR2 d, f). Where possible, all cores were independently oriented *in situ* using both magnetic and sun compasses. The differences between the two readings is limited to ±2°; hence, we assume local magnetic declination corrections are unnecessary.

A total of 262 samples from 43 sites at the Sangri County location were collected during two field campaigns: Sites TSa05-TSa41 were collected in 2011 (samples are labeled with letters "TSa") and Sites TSC01-TSC21 in 2012 (samples are labeled with letters "TSC"). Petrologies from the Sangri County location consist of intermediate basaltic andesites and andesites (Table DR1.1, DR1.2, DR1.3, and DR1.4; Figure DR2 a-f). We collected another 296 samples from 33 sites at the Sangye Town location. Sites TSa42-TSa67 were collected in 2011, and Sites TSC22-TSC40 were collected in 2012. Petrologies from the Sangye Town location also consist of intermediate basaltic andesites and andesites (Table DR2, DR4.1, DR4.2; Figure DR2 a-f).

A2. Zircon Uranium-Lead Geochronology

Geochronologic samples were prepared using standard crushing and heavy liquid separation techniques at the Center for Rocks and Minerals Separation in Langfang, Hebei province, China. Forty-one prismatic zircon grains from sample 2011TS06-11 and another 23 grains from sample 2011TS06-07 were hand-picked and mounted on adhesive tape, enclosed in epoxy resin and then polished to approximately half of their initial size. Cathode- Cathode-luminescence (CL) images of zircon grains (Figure DR3) were collected using a Gatan mini-CL detector attached to a JEOL JXA-8100 electron microprobe at the Institute of Geology and Geophysics, Chinese Academy of Sciences

(IGGCAS) in Beijing, China. Isotopes of ^{204}Pb, ^{206}Pb, ^{207}Pb, ^{232}Th and ^{238}U were collected using a Nd: YAG 213 laser ablation system (Microprobe 2, New Wave Research, U.S.A.) coupled to a VG PQ Excel ICP-MS. We used a laser repetition rate of 10 Hz, laser energy of 8-10 J/cm^2, and a focused laser beam that varied from 20 to 35 μm in diameter depending on the dimensions of the individual grains. Refer to Xia et al. (2006) for more details. We used zircon standard 91500 as our primary standard and GJ-1 as our secondary standard (Wiendenbeck et al., 1995; Jackson et al., 2004).

We used the GLITTER 4.0 software to reduce the mass spectrometer data (Griffin et al., 2008). Ages have been calculated from the U and Th decay constants recommended by Steiger and Jäger (1977). All reported common Pb corrections (using the ComPbCorr# routine), age calculations, and concordia diagrams were made using Isoplot 4.0 (Ludwig, 2012). The weighted $^{206}Pb/^{238}U$ ages of standard zircon 91500 and standard zircon GJ-1 obtained in this study are 1080±46 Ma (1 sigma, n=18), and 600±14 Ma (1 sigma, n=42), respectively, in agreement with the recommended values (Wiendenbeck et al., 1995; Jackson et al., 2004). Concordia plots for both samples suggest that there is very little or no Pb loss in our samples. Individual analyses for each sample are reported in the data table and Concordia plots with 1σ error and uncertainties in calculated ages are at the 95% level (2σ) (Appendix Figure DR4; Table DR1).

Zircon grains from sample 2011TS06-07 have $^{238}U/^{232}Th$ ratios greater than 0.74, with a maximum value of 2.17, which indicate minimum alteration by metamorphism. Of 23 analyses completed, 13 are nearly concordant and yield a weighted mean age of 179.9±7.2 Ma (MSWD=0.33) (Appendix Figure DR4 a, b; Table DR1). The 41 analyses from sample 2011TS06-11 have $^{238}U/^{232}Th$ ratios greater than 0.6 with a maximum value of 4.32. Of the 41 spot analyses completed, 26 are or nearly are concordant and yield a weighted mean age of 181.7±5.4 Ma (MSWD=2.1) (Appendix Figure DR4 c, d; Table DR1). Thus, the age of the Sangri Group lavas at the Sangri County location is ~180 Ma.

A3. Petrography

We analyzed thin sections of the Sangri Group lavas to identify textural relationships and diagenetic conditions of magnetic minerals. We completed standard transmitted and reflected light microscopy, as well as scanning electron microscopy (SEM) using a ZEISS EVO MA 10 SEM operating at 20 keV and 40-60 nA; the SEM was equipped with an Oxford Instruments energy dispersive spectrometer (EDS). All microscopy was conducted at the Key Laboratory of Continental Collision and Plateau Uplift (LCPU), ITPCAS.

A3.1 Polarized and Reflected Light Microscopy

Magnetite clearly coexists with feldspar and hornblende in many of our samples (Figures DR5, DR6). We do not observe degraded mineral margins in many samples, which suggests that these lavas have not experienced low-grade metamorphism, penetrative weathering, or both. A few specimens, however, do show textures consistent with secondary mineralization (Figure DR5, DR6); notably, titanohematite crystals are concentrated along margins of primary framework minerals and appear to be alteration products of feldspar and pyroxene (Figure DR5, DR6). These observations are supported and demonstrated more clearly by SEM analyses.

A3.2 Scanning Electronic Microscopic (SEM) Observations

Additional textural information about the iron oxides can be revealed by SEM observations. Both titanomagnetite and titanohematite are present in our samples, but with varying abundances which we divided into two general subpopulations. The first group contains samples 2011TS26-19, 2011TS27-14, -22, and -32, and is characterized by abundant titanomagnetite grains and few, if any, Ti-rich titanohematite grains. Titanomagnetite crystals usually occur as subhedral to euhedral grains ranging in size from a few micrometers up to 100 μm (Figures DR5b, c, e, f, h, i, j, k, l). These textures

show a typical magmatic origin (Craig, 2001; Turner et al., 2008).

The other group of samples (e.g., 2011TS26-12 and 2011TS26-13; Figure DR6) is characterized by titanomagnetite particles lacking oxidation-exsolution textures. Titanohematite in these samples is usually fine-grained and occurs either intergrown within titanomagnetite grains (Figure DR5b, c, e, f, h, i), around the silicate minerals (Figures DR6j, k, l), or along folia within the matrix and larger rock-forming minerals like feldsoar and pyroxene (Figures DR6c, g, l, o).

These petrographic observations suggest that titanomagnetite particles have a magmatic (*i.e.*, primary) origin, whereas titanohematite particles are most likely secondary and formed by weathering or low-temperature alteration. Notably, optical petrography and SEM images indicate that titanomagnetite is the predominant iron oxide for specimens with a high-temperature ChRM direction (Section A5).

A4. Rock Magnetism

Several rock-magnetic investigations of representative specimens were completed in order to identify and characterize the compositions and grain sizes of dominant remanence carriers. Residual chips collected from cuttings of paleomagnetic specimens were crushed into smaller fragments and powders for thermomagnetic runs, hysteresis measurements, FORC diagrams, and IRM acquisition curves.

A4.1. Low-field Susceptibility vs. Temperature (χ-T)

We measured low-field magnetic susceptibility (χ-T) as a function of temperature using an AGICO KLY-3S Kappabridge coupled to a CS-3 furnace. All thermomagnetic experiments were conducted in ambient atmosphere and measurements were collected continuously from room temperature up to 700°C and then back to room temperature from the peak temperature (Figure DR7). Cooling curves for all specimens except TSC01-8 and TSC39-8 are higher than heating curves (Figure DR7 a, b, d, f). Specimens

TSC18-2, TSC29-8, and TSa34-6 have approximately 20% higher susceptibility after cooling to room temperature than before heating; in contrast, specimen TSa37-3 shows a >50% susceptibility increase after heating. This increase in magnetic susceptibility is often caused by newly formed magnetic minerals, which can be attributed to exsolution of titanomagnetite into magnetite and ulvöspinel, by thermal alteration of authigenic clays, or by changes in magnetic grain sizes (Dunlop and Özdemir, 1997). Here we attribute the substantial increase of susceptibility after heating to exsolution of titanomagnetite into magnetite and ulvöspinel. χ-T heating-cooling curves for all samples show a decrease in magnetic susceptibility at or near ~580°C, ~675°C, or both (Figure DR7), indicating the presence of both Ti-poor titanomagnetite and Ti-poor titanohematite. This conclusion is consistent with the petrography described above and stepwise thermal demagnetization behavior of natural remanent magnetization (NRM) of specimens (Section A5 and Figure DR12 below), which shows that the maximum unblocking temperatures are reached by 540-680°C. Some specimens exhibit much lower χ-T changes and blocking temperatures, consistent with Ti-rich titanomagnetite and titanohematite. These specimens are few, however, and are not presented.

A4.2. Magnetic Hysteresis

One specimen per sampling site was selected for magnetic hysteresis measurements. We used a Princeton Measurements Corporation 3900 VSM with a maximum applied field of 1.8 T and a measurement averaging time of 100 ms.

Hysteresis curves display a variety of shapes, from slightly wasp-waisted, to narrow and rapidly saturating (most curves), to slightly pot-bellied, highlighting a mixture of coercivities and magnetic grain sizes (Tauxe et al., 1996; 2003) (Figure DR8). A Day plot of hysteresis parameters (Day et al., 1977) indicates that most specimens have psuedosingle domain (PSD) behavior (Figure DR9), which could be due to mixing between single-domain (SD) and multidomain (MD) subpopulations (Dunlop, 2002a, b) or strained domain states (vortex or flower structures (Tauxe et al., 2003)). Regardless

of the exact explanation for the PSD behavior, Sangri Group volcanics are predicted to be able to carry a stable remanence. A few specimens from both localities, however, have hysteresis values consistent with a mixture of SD and superparamagnetic (SP) titanomagnetite grains (Dunlop, 2002a, b), an observation that is consistent with the rapid magnetic saturation observed in some curves; these results could indicate weathering of primary Fe-oxides in these few specimens.

A4.3. First Order Reversal Curve (FORC) Diagrams

We calculated first order reversal curve (FORC) diagrams (Roberts et al., 2014) for ten specimens. For each specimen, 120 FORCs were measured in a saturating field of 1.5 T with an averaging time of 100 ms/step using the same VSM used for hysteresis measurements. FORCs were processed with FORCinel v6.04 (Harrison & Feinberg, 2008) and resulting FORC diagrams are shown in Figure DR10. Like the hysteresis curves displayed above, FORC diagrams for the Sangri Group lavas are varied. Most diagrams (Figure DR10, Samples TSa15-5, TSa34-6, TSa49-8, TSa53-7; TSC39-8, and TSC41-5) display a low coercivity population (<20 mT) with moderate to large symmetrical spread along the interaction axis and show patterns suggestive of a mixture of SD and small MD titanomagnetite grains (Muxworthy & Dunlop, 2002). This is consistent with the PSD grains inferred from the Day plot described above (Dunlop, 2002a,b). We also observe FORC diagrams that display weak magnetic interacting fields and high coercivities (Figure DR10, specimens TSa06-8 and TSC28-6), behavior that is similar to that expected of dispersed SD grains. A few specimens (*e.g.*, TSa16-8) display a relatively symmetrical and narrow H_u range, consistent with weak interaction fields and which may indicate the presence of PSD grains or a population of grains near the limit between SD and PSD particle (Pike et al., 1999; Roberts et al., 2000).

A4.4 Isothermal Remanent Magnetization (IRM) Acquisition Curves

We also measured IRM acquisition and backfield curves with the VSM, using a peak applied field of 1.8T. One specimen from each sample site was studied, and results generally fall into one of two categories. In the first, specimens saturate rapidly below 200 mT and have coercivities of remanence values (B_{cr}) ranging from 20-60 mT (Figure DR11). In the other, samples saturate only near or above 1.8 T and have B_{cr} values as high as ~350 mT (Figure DR11). The IRM acquisition curves are consistent with a predominance of titanomagnetite with some titanohematite. Petrographic relationships suggest these minerals are primary.

A5. Demagnetization of Natural Remanent Magnetization (NRM)

A5.1. Paleomagnetic Procedures

Paleomagnetic samples were cut into standard cylindrical specimens (2.2 cm long with diameter of 2.5 cm). All prepared specimens were subjected to stepwise thermal demagnetization using an ASC TD-48 thermal demagnetizer. Natural remanent magnetization (NRM) and subsequent remanent magnetizations after each demagnetization step for all samples were measured using a 2G Enterprises SQUID cryogenic magnetometer model 755R installed in a shielded room with a residual field less than 300 nT. These analyses were completed at the Paleomagnetism and Geochronology Laboratory (PGL), Institute of Geology and Geophysics, Chinese Academy of Sciences (IGGCAS) in Beijing. The NRM intensity of samples from several sites exceeded the measuring limit of the magnetometer at the PGL; in these situations, we measured the stepwise thermal demagnetization using an AGICO JR-6 spinner magnetometer installed at the Paleomagnetism and Environmental Magnetism laboratory (PMEM) at China University of Geosciences, Beijing. Like at the PGL, an ASC TD-48 oven was used to heat and cool the specimens. We designed our demagnetization

schemes following the results of our thermomagnetic studies, and each specimen was thermally demagnetized with 20-25 steps until the maximum unblocking temperature was approached.

Paleomagnetic data were analyzed and plotted using the online paleomagnetic analysis tools on www.paleomagnetism.org (Koymans et al., 2016), PMGSC software (written by Randy Enkin), and PaleoMac (Cogné, 2003) package. We evaluated our results using demagnetization curves projected onto orthogonal vector plots (Zijderveld, 1967), and distinct components were defined using principal component analysis (PCA) (Kirschvink, 1980). Most specimens record two magnetization components (*e.g.*, Figure DR12a, b, c, d, g, h, k, p, r), but some record only one distinct component (*e.g.*, Figure DR12 e, f, m, n, s, t, u). Some demagnetization data defined arcuate demagnetization paths, and in these cases we used the great circle method to define the characteristic direction (Halls, 1978).

Site mean directions were calculated using Fisher statistics (Fisher 1953) or the McFadden and McElhinny (1988) approach that combines directions and great circles. We calculated site mean directions using only characteristic remanent magnetizations (ChRMs) that are fit by at least 4 consecutive demagnetization steps and have maximum angular deviations (MAD) values equal to or less than 15° (Table DR4.1-DR4.2). Ideally, site mean directions are calculated following criteria listed as below, 1) Fisherian mean calculated from at least 3 ChRM directions/great circles and 2) A value of the precision parameter k larger than 50. Sixty-two lava sites meet our quality criteria, of which two fall outside a 45° cutoff angle around the mean direction: these data provide an average direction of $D \pm \Delta D = 339.8 \pm 3.4°$, $I \pm \Delta I = -7.4 \pm 6.7°$, $A95 = 3.4°$, $K = 30.1$, $n=60$.

A5.2 Paleomagnetic Results

Samples from several sites (Sites TSa5, TSa14, TSa16, TSa19) have especially high NRM intensities. Generally, we distinguish two remanence components according to their demagnetization behavior and directions isolated in each specimen. For convenience, we refer to them as Component A and Component B respectively.

Component A is usually isolated at treatment levels from 80/100°C-300-350°C; we therefore also refer to it as a low temperature component (LT). This component could be isolated from a portion of samples (~40%) and usually displays a downward, northerly direction before bedding correction (Figures DR12, DR13a, b). Component A directions cluster around the present geomagnetic field (PGF) and present dipole field (PDF) (D=358.5°, I=46.5°), consistent with a viscous origin or overprint superimposed on the ChRM direction (Figure DR13a, b).

Component B was successfully isolated in most specimens (Figure DR12; Table DR4.1-DR4.2). This component is defined from approximately 350°C up to 580°C or 660°C, decays toward the origin and is regarded as the ChRM. Tilt-corrected directions are either upward and northerly or downward and southerly and are generally antipodal (Table DR4.1, DR4.2).

References for Supplemental Information

Andersen, T., 2002. Correction of common lead in U-Pb analyses that do not report Pb-204. Chemical Geology 192, 59-79.

Appel E., Müller, R., Widder R., 1991. Palaeomagnetic results from the Tibetan Sedimentary Series of the Manang area (north central Nepal). Geophysical Journal International 104, 255-266.

Chen, W.W., Yang, T.S., Zhang, S.H., Yang, Z.Y., Li, H.Y., Wu, H.C., Zhang, J.H., Ma, Y.M., Cai, F.L., 2012. Paleomagnetic results from the early Cretaceous Zenong Group volcanic rocks, Cuoqin, Tibet, and their paleogeographic implications. Gondwana Research 22, 461-469.

Crouzet, C., Gautam, P., Schill, E., Appel, E., 2003. Multicomponent magnetization in western Dolpo (Tethyan Himalaya, Nepal): tectonic implications. Tectonophysics 377, 179-196.

Cogné, J.P., 2003. PaleoMac: a Macintosh™ application for treating paleomagnetic data and making plate reconstructions. Geochemistry, Geophysics Geosystems 4, 1007, doi: 10.1029/2001GC000227.

Craig, J.R., 2001. Ore-Mineral Textures and the Tales They Tell. The Canadian Mineralogist 39, 937-956, doi: 10.2113/gscanmin.39.4.937.

Day, R., Fuller, M., and Schmidt, V., 1977. Hysteresis properties of titanomagnetites: grain-size and compositional dependence. Physics of the Earth and Planetary Interiors 13, 260-267.

Ding, J.K., Zhang, S.H., Chen, W.W., Zhang, J.H., Yang, T.S., Jiang, G.L., Zhang, K.X., Li, H.Y., Wu, H.C., 2014. Paleomagnetism of the Oligocene Kangtuo Formation red beds (central Tibet): Inclination Shallowing and tectonic implications. Journal of Asian earth Sciences 104, 55-68.

Dong, X.B., Wang, Z.M., Tan, C.Z., Yang, H.X., and Cheng, L.R., 1991. New results of paleomagnetic studies of the Qinghai-Tibetan plateau. Geological Review 37, 160–164.

Dunlop, D.J., and Özdemir, Ö., 1997. Rock magnetism: Fundamentals and Frontiers.

285 Cambridge Studies in Magnetism. Cambridge University Press. Cambridge.
286 Dunlop, D.J., 2002a. Theory and application of the Day plot (Mrs/Ms versus Hcr/Hc) 1.
287 Theoretical curves and tests using titanomagnetite data. Journal of Geophysical
288 Research 107, 2056, doi: 10.1029/2001JB000486.
289 Dunlop, D.J., 2002b.Theory and application of the Day plot (Mrs/Ms versus Hcr/Hc) 2.
290 Application to data for rocks, sediments, and soils. Journal of Geophysical Research
291 107, 2057, doi: 10.1029/2001JB000487.
292 Dupont-Nivet, G., van Hinsbergen, D.J.J., Torsvik, T., 2010. Persistently low Asian
293 paleolatitudes: Implications for the India-Asia collision history. Tectonics 29, TC5016,
294 doi: 10.1029/2008TC002437.
295 Fisher, R.A., 1953. Dispersion on a sphere. Proc. R. Soc. Lond., A217, 295-305.
296 Griffin, W.L., Powell, W.J., Pearson, N.J., 2008. GLITTER: data reduction software for laser
297 ablation ICP-MS. In: Laser Ablation-ICP-MS in the earth sciences. Mineralogical
298 association of Canada short course series 40, 204-207.
299 Guo, Q., 2009, Research on Paleomagnetism of Gangdise Plate of Qinghai-Tibet Plateau
300 in Late Paleozoic. Northwest Universtiy Master's Dissertation.
301 Halls, H.C., 1978. The use of converging remagnetization circles in palaeomagnetism.
302 Physics of the Earth and Planetary Interiors 16, 1-11.
303 Harrison, R.J., and Feinberg, J.M., 2008. FORCinel: An improved algorithm for calculating
304 first-order reversal curve distributions using locally weighted regression smoothing.
305 Geochemistry Geophysics Geosystems 9, A05016, doi:10.1029/2008GC001987.
306 Huang, W.T., Dupont-Nivet, G., Lippert, P.C., van Hinsbergen, D.J.J., and Hallot, E., 2013.
307 Inclination shallowing in the Eocene Linzizong sediments from Tibet: correction,
308 possible causes and implications for reconstructing the India-Asia collision.
309 Geophysical Journal International 194, 1390-1411.
310 Huang, W.T., Dupont-Nivet, G., Lippert, P.C., van Hinsbergen, D.J.J., Dekkers, M.J., Guo, Z.,
311 Waldrip, R., Li, X., Zhang, X., Liu, D., and Kapp, P., 2015a, Can a primary paleolatitude
312 be retrieved from partially remagnetized Eocence volcanics in the Nanmulin Basin
313 (Southern Tibet) to date the India-Asia collision?, Journal of Geophysical Research
314 120, 42-66.

315 Huang, W.T., van Hinsbergen, D.J.J., Maffione, M., Orme, D., Dupont-Nivet, G., Guilmette, C.,
316 Ding, L., Guo, Z., and Kapp, P., 2015b. Lower Cretaceous Xigaze ophiolites formed in
317 the Gangdese forearc: evidence from paleomagnetism, sediment provenance, and
318 stratigraphy. Earth and Planetary Science Letters 415, 142-153.
319 Huang, W.T., van Hinsbergen, D.J.J., Dekkers, M.J., Garzanti, E., Dupont-Nivet, G., Lippert,
320 P.C., Li, X., Maffione, M., Langereis, C.G., Hu, X., Guo, Z., and Kapp, P., 2015c,
321 Paleolatitudes of the Tibetan Himalaya from primary and secondary magnetizations
322 of Jurassic to Lower Cretaceous sedimentary rocks, Geochemistry Geophysics
323 Geosystems 16, 77-100.
324 Jackson, S.E., Pearson, N.J., Griffin, W.L., Belousova, E.A., 2004. The application of laser
325 ablation-inductively coupled plasma-mass spectrometry to in situ U–Pb zircon
326 geochronology. Chemical Geology 211, 47-69.
327 Kirschvink, J.L., 1980. The least-square line and plane and the analysis of paleomagnetic
328 data. Geophys. J. R. Astron. Soc. 62, 699-718.
329 Klootwijk, C.T., and Bingham, D.K., 1980. The extent of greater India, III. Palaeomagnetic
330 data from the Tibetan Sedimentary series, Thakkhola region, Nepal Himalaya. Earth
331 and Planetary Science Letters 51, 381-405.
332 Klootwijk, C.T., Shah, S.K., Gergan, J., Sharma, M.L., Tirkey, B., Gupta, B.K., 1983. A
333 palaeomagnetic reconnaissance of Kashmir, northwestern Himalaya, India. Earth and
334 Planetary Science Letters 63, 305-324.
335 Koymans, M.R., Langereis, C.G., Pastor-Galán, D., van Hinsbergen, D.J.J., 2016.
336 Paleomagnetism.org: An online multi-platform open source environment for
337 paleomagnetic data analysis. Computers and Geosciences, In Press.
338 Lippert, P.C., van Hinsbergen, D., and Dupont-Nivet, G., 2014, Early Cretaceous to present
339 latitude of the central proto-Tibetan Plateau: A paleomagnetic synthesis with
340 implications for Cenozoic tectonics, paleogeography, and climate of Asia: Geological
341 Society of America Special Paper 507, 1–21, doi: 10.1130/2014.2507(01).
342 Ludwig, K.R., 2003. Isoplot 3.00: Berkeley Geochronology Center Special Publication 4,
343 pp. 70.
344 Ma, Y.M., Yang, T.S., Yang, Z.Y., Zhang, S.H., Wu, H.C., Li, H.Y., Li, H.K., Chen, W.W., Zhang, J.H.,

and Ding, J.K., 2014. Paleomagnetism and U-Pb zircon geochronology of Lower Cretaceous lava flows from the western Lhasa terrane: New constraints on the India-Asia collision process and intracontinental deformation within Asia. Journal of Geophysical Research 119, doi:10.1002/2014JB011362.

McFadden, P.L., McElhinny, M.W., 1988. The combined analysis of remagnetization circles and direct observations in paleomagnetism. Earth and Planetary Science Letters 87, 161-172.

Muxworthy, A. R., and Dunlop, D.J., 2002. First-order reversal curve (FORC) diagrams for pseudo-single-domain magnetites at high temperature, Earth and Planetary Science Letters 203(1), 369-382, doi:10.1016/s0012-821x(02)00880-4.

Patzelt, A., Li, H.M., Wang, J.D., Appel, E., 1996. Paleomagnetism of Cretaceous to Tertiary sediments from southern Tibet: evidence for the extent of the northern margin of India prior to the collision with Eurasia. Tectonophysics 259, 259-284.

Pike, C.R., Roberts, A.P., and Verosub, K.L., 1999. Characterizing interactions in fine magnetic particle systems using first order reversal curves. Journal of Geophysical Research 85, 6660-6667.

Ran, B., Wang, C., Zhao, X., Li, Y., He, M., Zhu, L., and Coe, R.S., 2012, New paleomagnetic results of the early Permian in the Xainza area, Tibetan Plateau and their paleogeographical implications. Gondwana Research, 22, 447-460, doi: 10.1016/j.gr.2011.11.014.

Roberts, A.P., Heslop, D., Zhao, X., and Pike, C.R., 2014. Understanding fine magnetic particle systems through use of first-order reversal curve diagrams. Reviews of Geophysics 52(4), 2014RG000462, doi:10.1002/2014RG000462.

Roberts, A.P., Pike, C.R., and Verosub, K.L., 2000. First-order reversal curve diagrams: a new tool for characterizing the magnetic properties of naural samples. Journal of Geophysical Research: solid earth 105, 28461-28475, doi: 28410.21029/22000JB900326.

Schilla, E., Appel, E., Gautamb, P., 2002. Towards pyrrhotite/magnetite geothermometry in low-grade metamorphic carbonates of the Tethyan Himalayas (Shiar Khola, Central Nepal). Journal of Asian Earth Sciences 20, 195-201.

375 Steiger, R.H., and Jäger, E., 1977. Subcommission on geochronology: convention on the
376 use of decay constants in geo-and cosmochronology. Earth and Planetary Science
377 Letters 36, 359-362.
378 Sun, Z.M., Pei, J.L., Li, H.B., Xu, W., Jiang, W., Zhu, Z.M., Wang, X.S., Yang, Z.Y., 2012.
379 Palaeomagnetism of late Cretaceous sediments from southern Tibet: Evidence for
380 the consistent palaeolatitudes of the southern margin of Eurasia prior to the
381 collision with India. Gondwana Research 21, 53-63.
382 Tan, X.D., Gilder, S., Kodama, K.P., Jiang, W., Han, Y.L., Zhang, H., Xu, H.H., Zhou, D., 2010.
383 New paleomagnetic results from the Lhasa block: Revised estimation of latitudinal
384 shortening across Tibet and implications for dating the India-Eurasia collision. Earth
385 and Planetary Science Letters 293, 396-404.
386 Tauxe, L., Mullender, T. A. T., and Pick, T., 1996. Potbellies, wasp-waists, and
387 superparamgnetism in magnetic hysteresis. Journal of Geophysical Research: Solid
388 Earth 101(B1), 571-583.
389 Tauxe, L., Bertram, H. N., and Seberino, C., 2003. Physical interpretation of hysteresis
390 loops: Micromagnetic modeling of fine particle magneite. Geochemisty Geophysics
391 Geosystems 3(10), 1055, doi:10.1029/2001GC000241.
392 Turner, M.B., Cronin, S.J., Stewart, R.B., Bebbington, M., and Smith, I.E.M., 2008. Using
393 titanomagnetite textures to elucidate volcanic eruption histories. Geology 36, 31-34,
394 doi: 10.1130/G24186A.1.
395 Xia, X.P., Sun, M., Zhao, G.C., Wu, F.Y., Xu, P., Zhang, J. H., Luo, Y., 2006. U–Pb and Hf isotopic
396 study of detrital zircons from the Wulashan khondalites: Constraints on the
397 evolution of the Ordos Terrane, Western Block of the North China Craton. Earth
398 Planet. Sci. Lett., 241, 581-593.
399 Wiedenbeck, M., Alle, P., Corfu, F., Griffin, W.L., Meier, M., Oberli, F., Von Quadt, A., Roddick,
400 J.C., and Spiegel, W., 1995. Three natural zircon standards for U-Th-Pb, Lu-Hf, trace
401 element and REE analyses. Geostandards Newsletter 19, 1-23.
402 Yang, T.S., Ma, Y.M., Zhang, S.H., Bian, W.W., Yang, Z.Y., Wu, H.C., Li, H.Y., Chen, W.W., Ding,
403 J.K., 2014. New insights into the India-Asia collision process from Cretaceous

paleomagnetic and geochronologic results in the Lhasa terrane. Gondwana Research, In Press, doi:10.1016/j.gr.2014.06.010.

Yang, T.S., Ma, Y.M., Bian, W.W., ,Jin, J.J.,, Zhang, S.H., Wu, H.C., LI, H.Y., Yang, Z.Y., Ding, J.K., 2015. Paleomagnetic results from the Early Cretaceous Lakang Formation lavas: Constraints on the paleolatitude of the Tethyan Himalaya and the India–Asia collision. Earth and Planetary Science Letters 428, 120-133.

Ye, X.H., and Li, J.F., 1987, Palaeomagnetismand evolution of Tibet plates and Tethys. Journal of Chengdu College of Geology 14, 65–79.

Yi, Z.Y., Huang, B.C., Chen, J.S., Chen, L.W., Wang, H.L., 2011. Paleomagnetism of early Paleogene marine sediments in southern Tibet, China: Implications to onset of the India-Asia collision and size of Greater India. Earth and Planetary Science Letters 309, 153-165.

Zijderveld, J.D.A., 1967. AC demagnetization of rocks: analysis of results. In: Collinson, D.W., Creer, K.M., Runcorn, S.K. (Eds.), Methods in Paleomagnetism. Elsevier, New York, pp. 254-286.

Zhu, Z.W., 1985, Comparative significance of apparent polar wander path of Xizang and its adjacent regions from Phanerozoic: Acta Geophyisa Sinica 28, 219–225 (Chinese with English Abstract).

Appendix Figures List

Figure DR1: Geologic map of sampling region.

Figure DR2: Field photographs of sampling region.

Figure DR3: Cathode-luminescence images of zircons.

Figure DR4: Weighted-mean ages and concordia plots of zircon U-Pb data.

Figure DR5: Photomicrograph collage 1.

Figure DR6: Photomicrograph collage 2.

Figure DR7: Low-field magnetic susceptibility *vs.* temperature curves.

Figure DR8: Hysteresis loops.

Figure DR9: Day plot of magnetic hysteresis parameters.

Figure DR10: FORC diagrams.

Figure DR11: IRM acquisition curves.

Figure DR12: Orthogonal vector plots of demagnetization data.

Figure DR13: Stereoplots of LTC and HTC directions and mean directions in IS and TC coordinates for Sangri County locality.

Appendix Tables List

Table DR1: U-Pb dating results for two bulk samples (2011TS06-7 and 2011TS06-11).

Table DR2: Information of thin sections used for optical petrography.

Table DR3.1: Summary of measured hysteresis parameters (For TSa samples).

Table DR3.2: Summary of measured hysteresis parameters (For TSC samples).

Table DR4.1: Summary of paleomagnetic sampling sites and directional statistics (TSa samples).

Table DR4.2: Summary of paleomagnetic sampling sites and directional statistics (TSC samples).

Table DR5.1: Selected and obtained paleopoles for reconstructing paleolatitude of the Lhasa block in Mesozoic.

Table DR5.2: Selected and obtained latest volcanic-based paleopoles for reconstructing paleolatitude of the Qiangtang block in Mesozoic.

Table DR5.3: Selected and obtained paleopoles for reconstructing paleolatitude of the Tethyan-Himalayan block in Mesozoic up to Cenozoic.

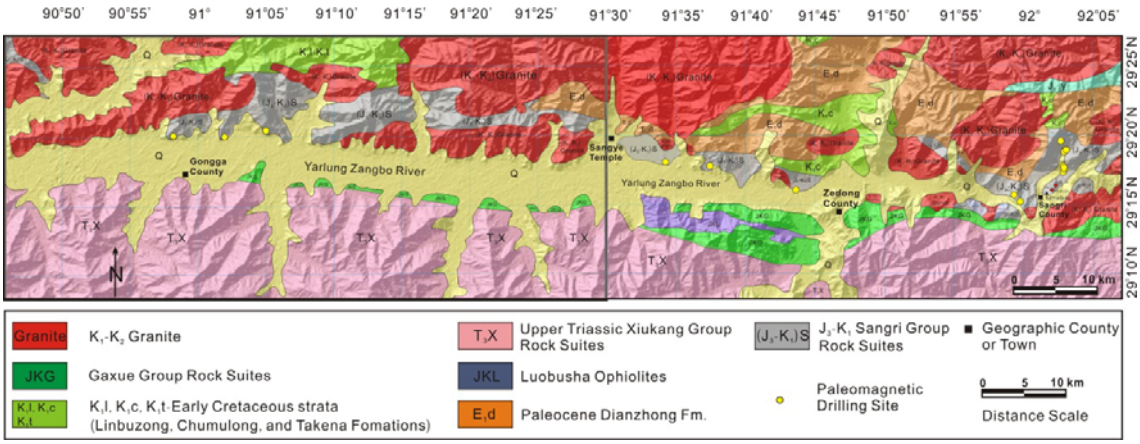

Figure DR1: Local geologic map around Sangri County and Sangye Town. Area in grey shows the distribution of the Sangri Group volcanics; yellow dots display the paleomagnetic drilling sites; two red dots at the Sangri County locality show the location of the geochronologic samples.

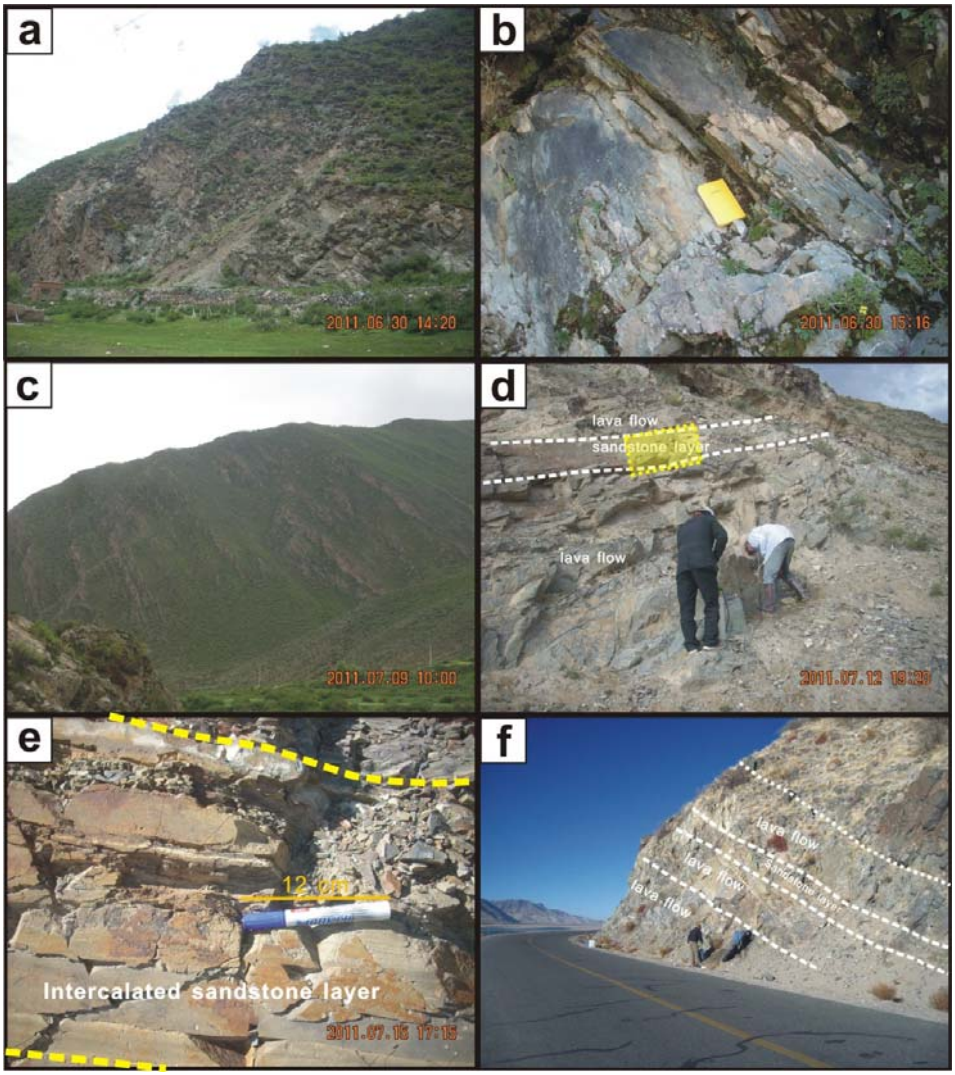

Figure DR2: Photographs of field localities. (**a**) Outcrops of the Sangri Group lavas (Sangri County locality, view is to the southeast); (**b**) Stratigraphic layering of the Sangri Group lavas (Sangri County locality, view is to the south); (**c**) Outcrops of limestone conformably beneath the Sangri Group lavas (Sangri County locality, view is to the northwest); (**d**) Planar lavas and intercalated sandstone layers (Sangye Town locality, view is to the northeast); area indicated in yellow shows the location of Fig. A1e; (**e**) Sandstone layers intercalated with lavas (view is to the north); (**f**) Fresh outcrops of layered lavas and intercalated sandstone beds at the Sangye Town locality; people for scale.

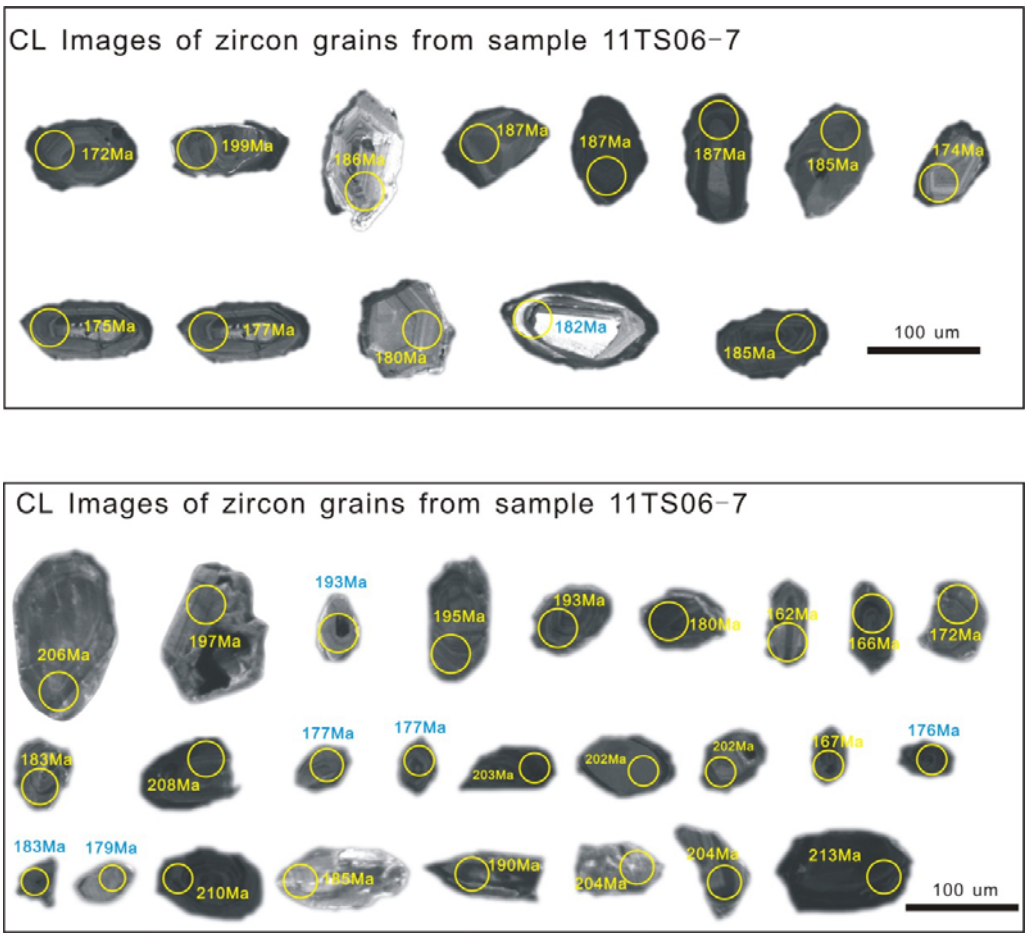

Figure DR3: Cathode-luminescence images of zircon grains used for LA-ICP-MS geochronology; spot locations and corresponding calculated U-Pb zircon ages shown.

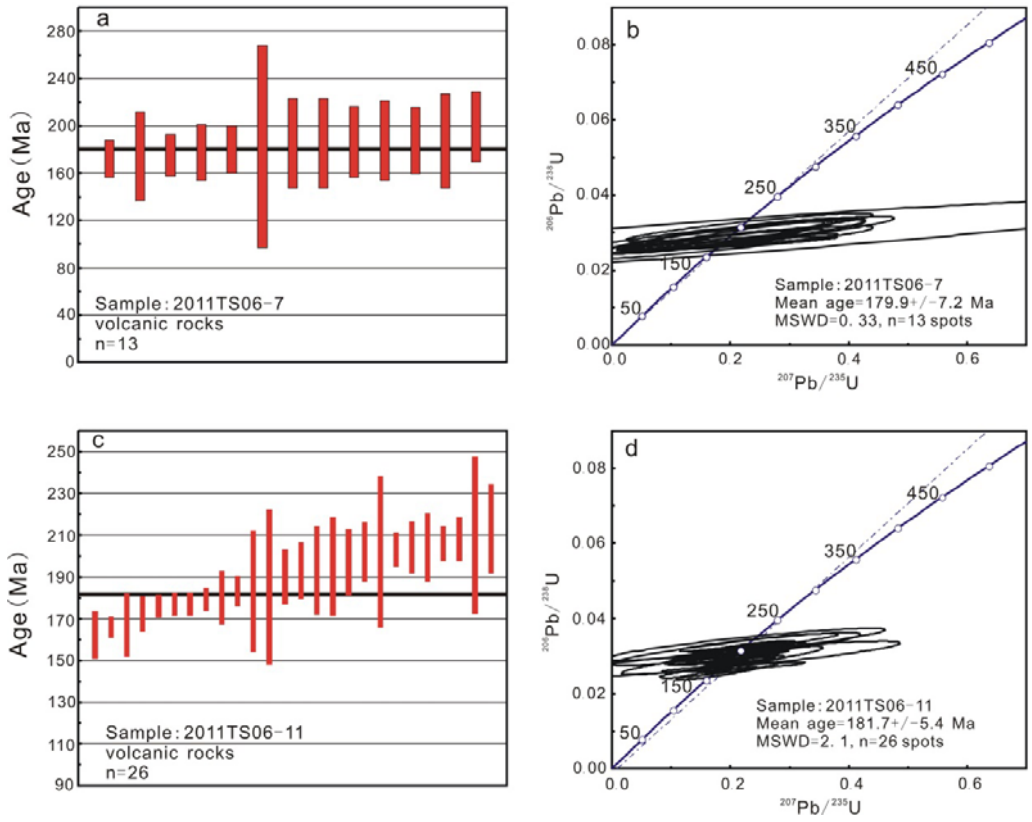

Figure DR4: Weighted mean age and concordia plots for geochronological samples. Left column shows the ages of individual zircon analyses and their weighted mean age; right column shows concordia plots. Analytical uncertainties are reported at the 2σ level and data are in Table DR1. Plots were made using Isoplot 4.0 (Ludwig 2012).

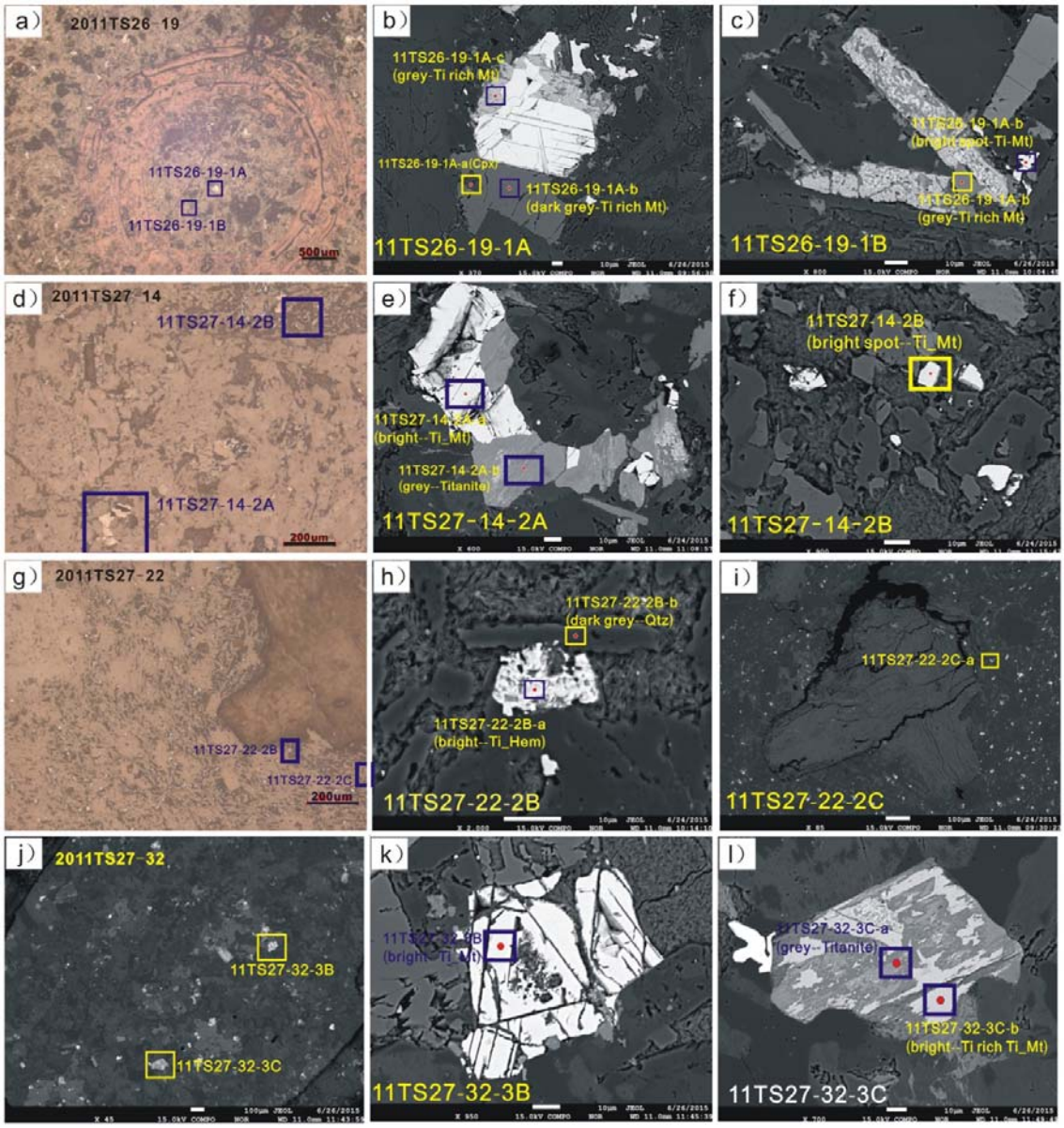

Figure DR5: Reflected light photomicrographs and SEM images of representative volcanic samples whose remanence carriers are Ti-rich and Ti-poor titanomagnetite. Subfigures a, b, g are photomicrographs taken under reflected light, whereas the remaining images show scanning electronic microscopic results.

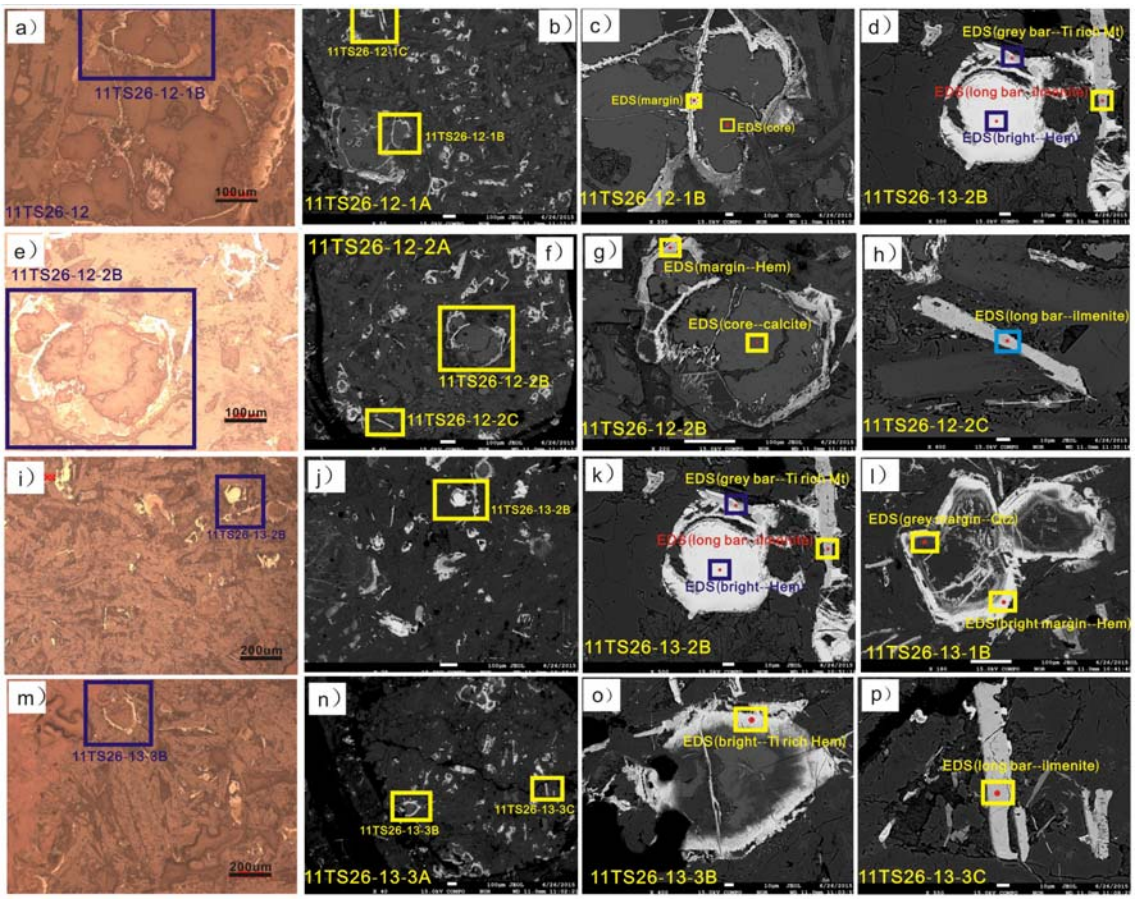

Figure DR6: Reflected light photomicrographs and SEM images of representative volcanic samples whose remanence carriers are Ti-rich and Ti-poor titanohematite. Subfigures a, e, i and m are photomicrographs taken under reflected light, whereas the remaining images show scanning electronic microscopic results.

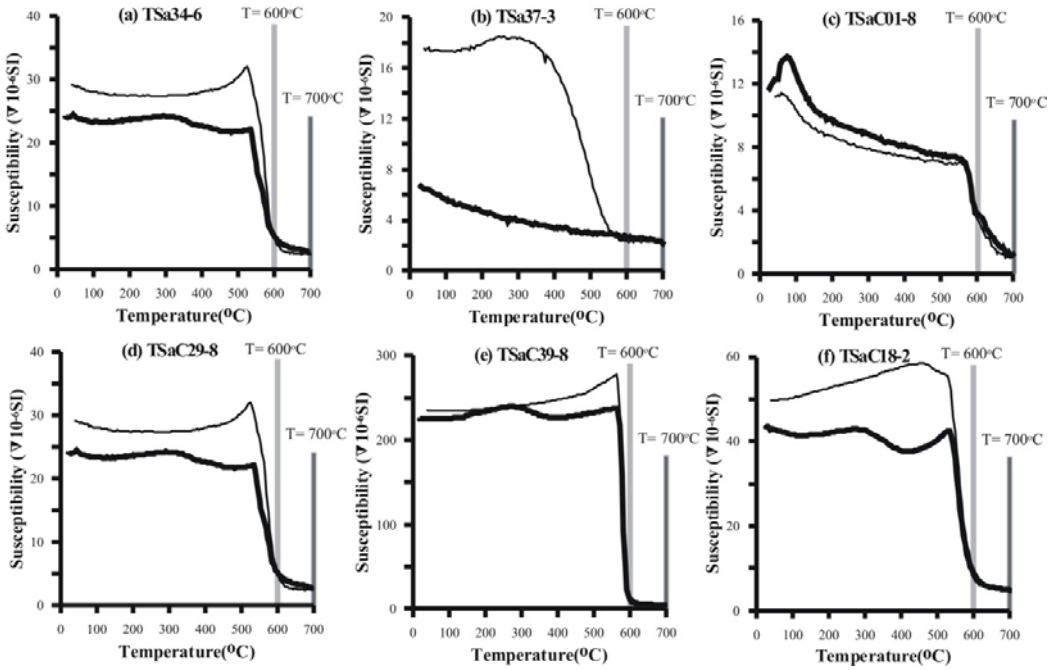

Figure DR7: Temperature-dependence of weak-field magnetic susceptibility. Thick black lines (thin black lines) show the heating (cooling) curves measured during heating from room temperature to 700°C and cooling back to room temperature in ambient air.

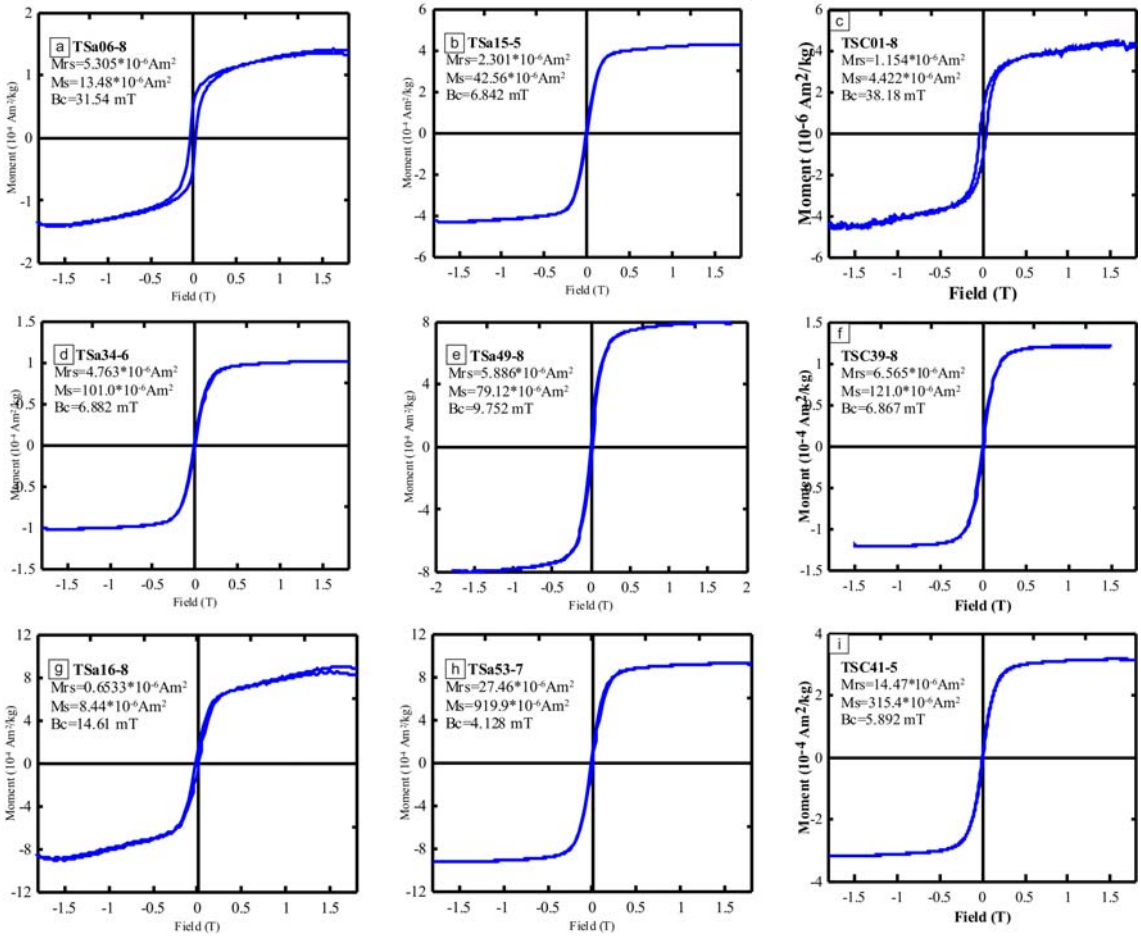

Figure DR8: Magnetic hysteresis loops for specimens from the Sangri Group volcanics.

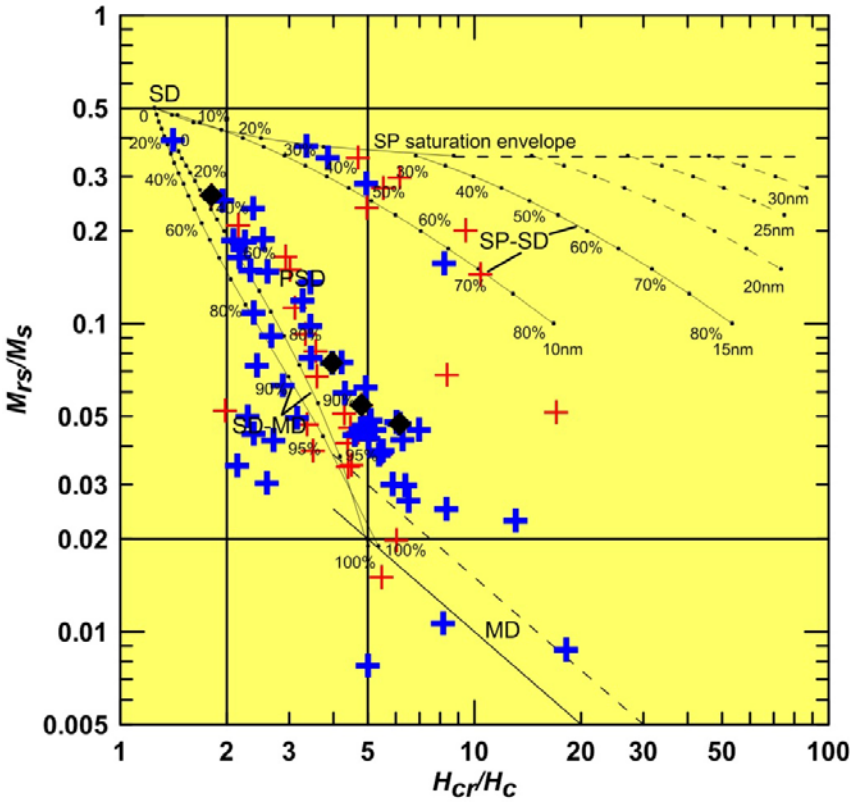

495

496 **Figure DR9:** Day plot (Day et al., 1977; Dunlop, 2002a) of hysteresis parameters for
497 specimens from Sangri Group volcanics. Blue crosses (52 specimens) indicate
498 specimens from the 2011 sampling campaign (both locations), whereas red crosses (29
499 speciemens) are specimens from the 2012 sampling campaign (both locations). Curves
500 show mixing lines between single domain (SD) and multidomain (MD) titanomagnetites
501 and between SD and superparamagnetic (SP) titanomagnteite, from Dunlop (2002a, b).
502 See Table DR3.1, DR3.2 and text described in A4.2 for more information.

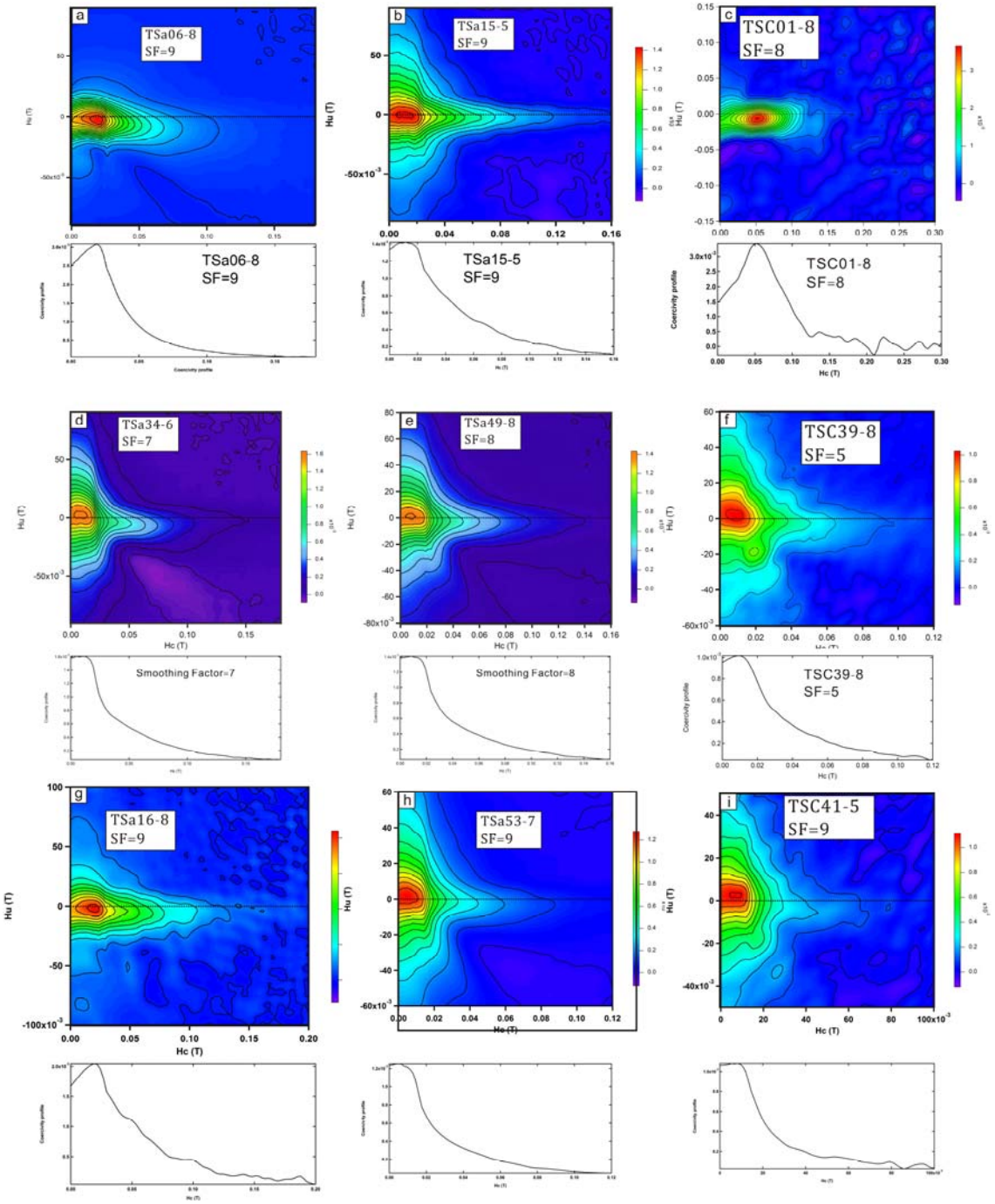

Figure DR10: First order reversal curve (FORC) diagrams for specimens from the Sangri Group volcanics. See text for details.

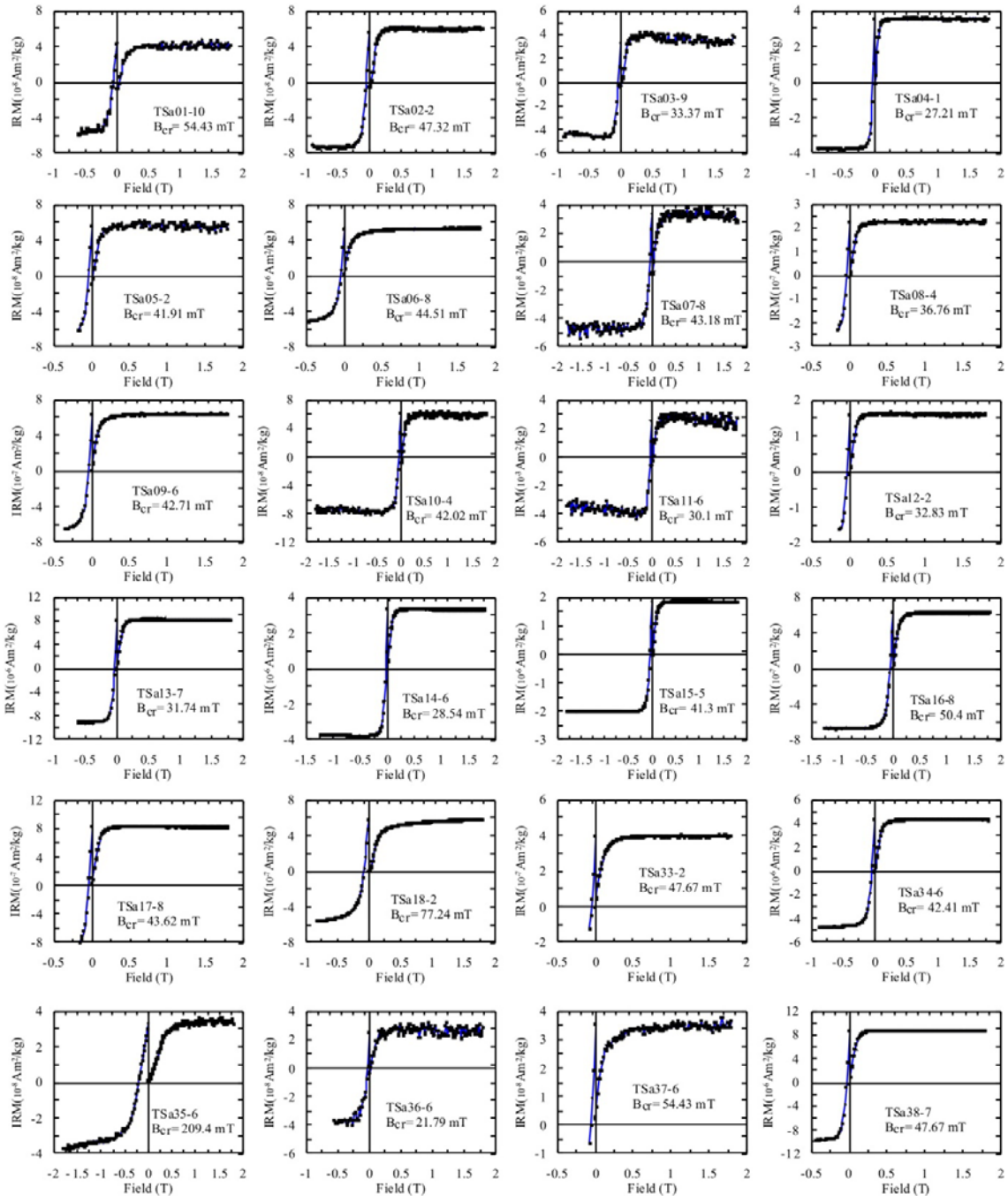
TSa01-10
Bcr= 54.43 mT
TSa02-2
Bcr= 47.32 mT
TSa03-9
Bcr= 33.37 mT
TSa04-1
Bcr= 27.21 mT
TSa05-2
Bcr= 41.91 mT
TSa06-8
Bcr= 44.51 mT
TSa07-8
Bcr= 43.18 mT
TSa08-4
Bcr= 36.76 mT
TSa09-6
Bcr= 42.71 mT
TSa10-4
Bcr= 42.02 mT
TSa11-6
Bcr= 30.1 mT
TSa12-2
Bcr= 32.83 mT
TSa13-7
Bcr= 31.74 mT
TSa14-6
Bcr= 28.54 mT
TSa15-5
Bcr= 41.3 mT
TSa16-8
Bcr= 50.4 mT
TSa17-8
Bcr= 43.62 mT
TSa18-2
Bcr= 77.24 mT
TSa33-2
Bcr= 47.67 mT
TSa34-6
Bcr= 42.41 mT
TSa35-6
Bcr= 209.4 mT
TSa36-6
Bcr= 21.79 mT
TSa37-6
Bcr= 54.43 mT
TSa38-7
Bcr= 47.67 mT
Field (T)

506

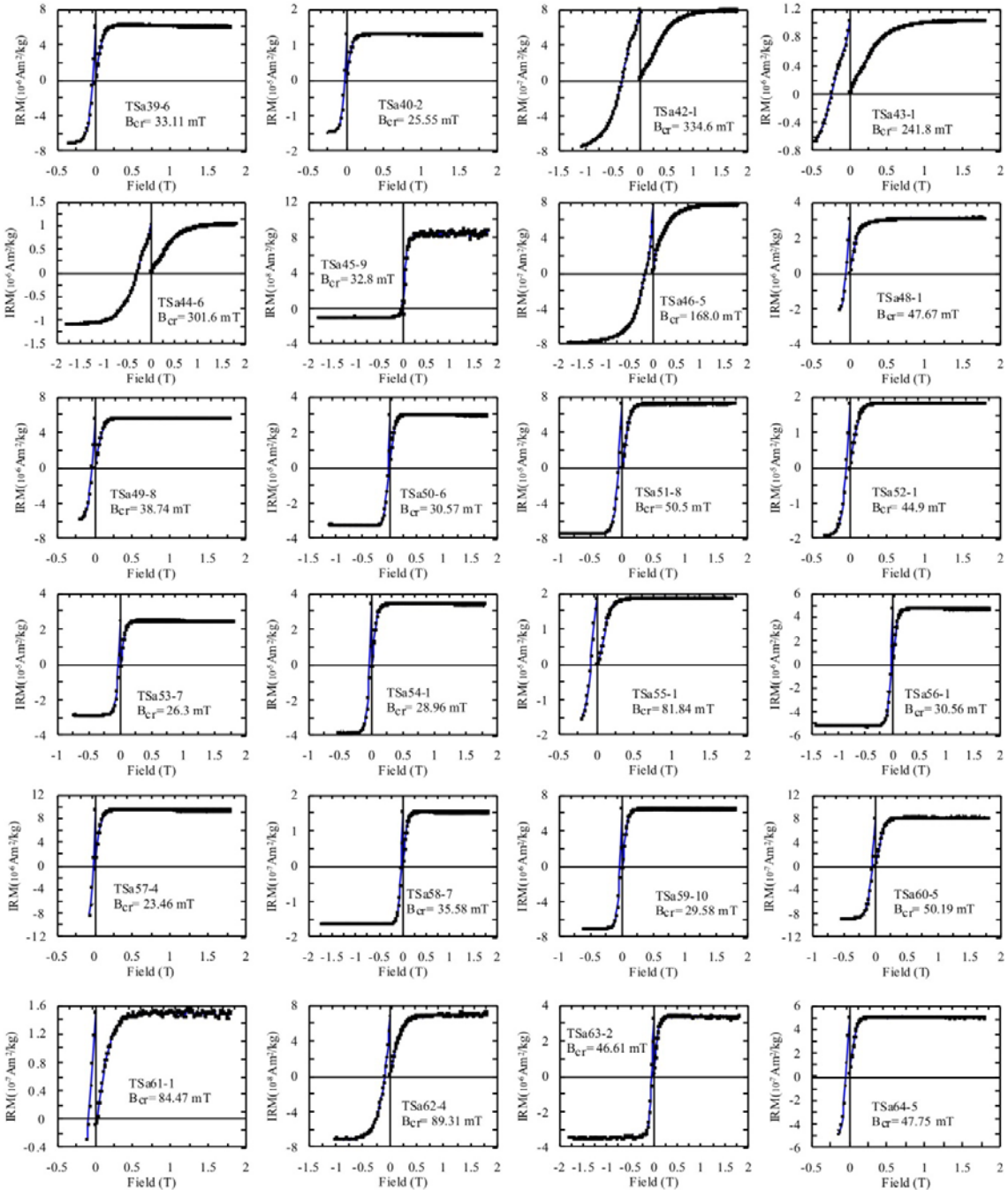
TSa39-6
Bcr= 33.11 mT
TSa40-2
Bcr= 25.55 mT
TSa42-1
Bcr= 334.6 mT
TSa43-1
Bcr= 241.8 mT
TSa44-6
Bcr= 301.6 mT
TSa45-9
Bcr= 32.8 mT
TSa46-5
Bcr= 168.0 mT
TSa48-1
Bcr= 47.67 mT
TSa49-8
Bcr= 38.74 mT
TSa50-6
Bcr= 30.57 mT
TSa51-8
Bcr= 50.5 mT
TSa52-1
Bcr= 44.9 mT
TSa53-7
Bcr= 26.3 mT
TSa54-1
Bcr= 28.96 mT
TSa55-1
Bcr= 81.84 mT
TSa56-1
Bcr= 30.56 mT
TSa57-4
Bcr= 23.46 mT
TSa58-7
Bcr= 35.58 mT
TSa59-10
Bcr= 29.58 mT
TSa60-5
Bcr= 50.19 mT
TSa61-1
Bcr= 84.47 mT
TSa62-4
Bcr= 89.31 mT
TSa63-2
Bcr= 46.61 mT
TSa64-5
Bcr= 47.75 mT
Field (T)

507

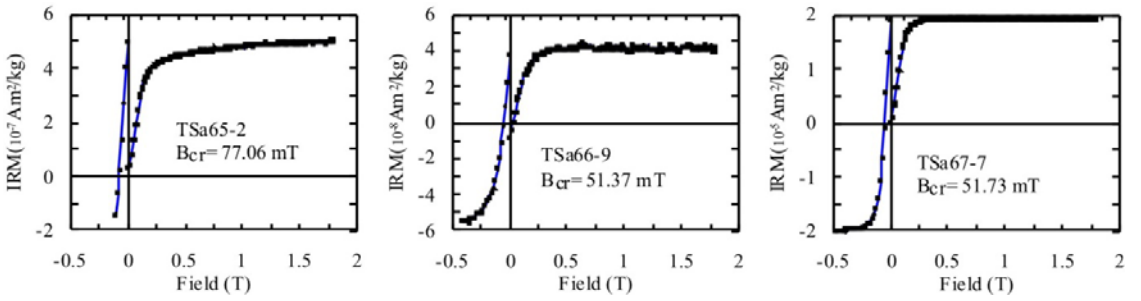
TSa65-2
Bcr= 77.06 mT
TSa66-9
Bcr= 51.37 mT
TSa67-7
Bcr= 51.73 mT
Field (T)

508

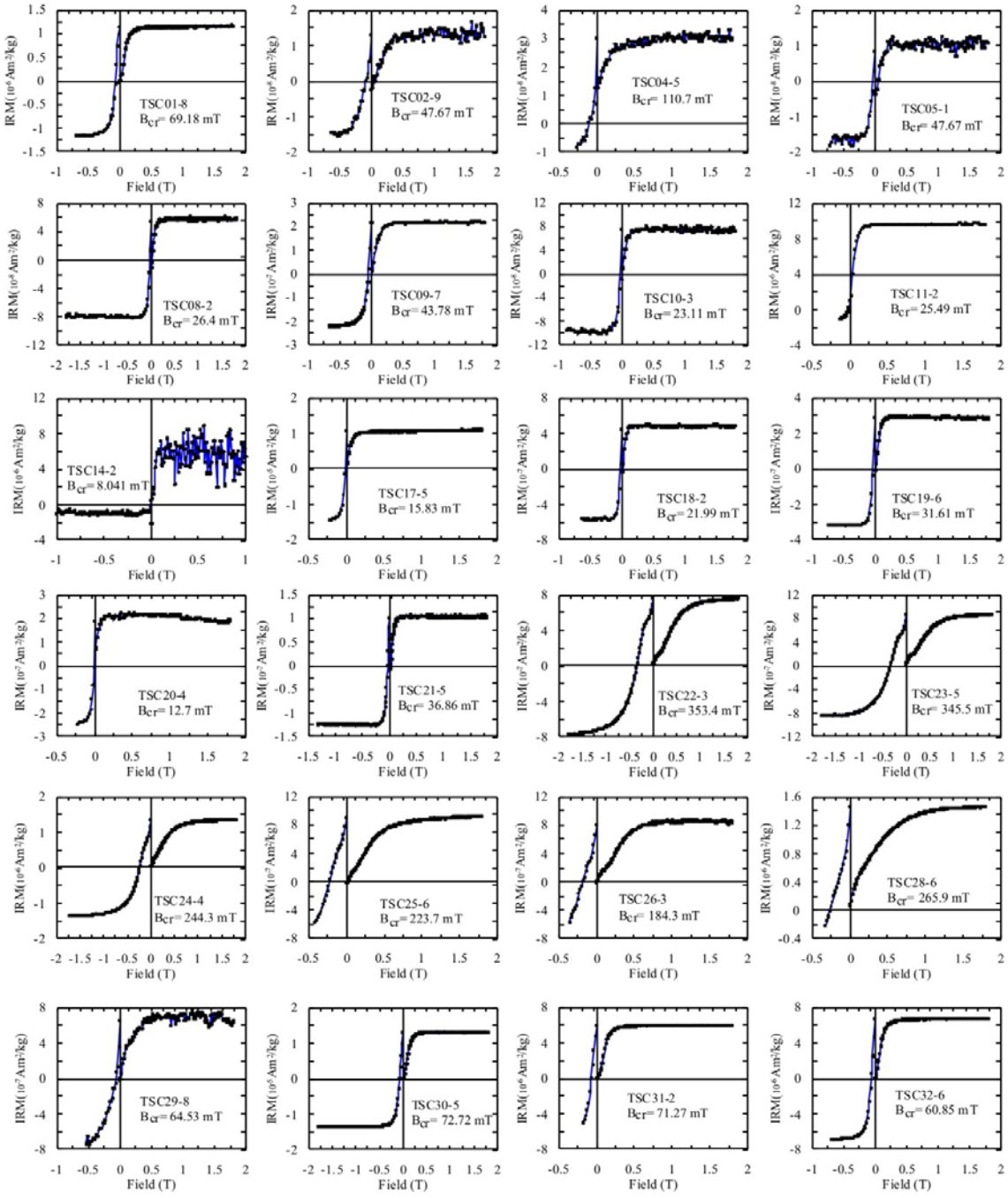
TSC01-8
Bcr= 69.18 mT
TSC02-9
Bcr= 47.67 mT
TSC04-5
Bcr= 110.7 mT
TSC05-1
Bcr= 47.67 mT
TSC08-2
Bcr= 26.4 mT
TSC09-7
Bcr= 43.78 mT
TSC10-3
Bcr= 23.11 mT
TSC11-2
Bcr= 25.49 mT
TSC14-2
Bcr= 8.041 mT
TSC17-5
Bcr= 15.83 mT
TSC18-2
Bcr= 21.99 mT
TSC19-6
Bcr= 31.61 mT
TSC20-4
Bcr= 12.7 mT
TSC21-5
Bcr= 36.86 mT
TSC22-3
Bcr= 353.4 mT
TSC23-5
Bcr= 345.5 mT
TSC24-4
Bcr= 244.3 mT
TSC25-6
Bcr= 223.7 mT
TSC26-3
Bcr= 184.3 mT
TSC28-6
Bcr= 265.9 mT
TSC29-8
Bcr= 64.53 mT
TSC30-5
Bcr= 72.72 mT
TSC31-2
Bcr= 71.27 mT
TSC32-6
Bcr= 60.85 mT
Field (T)

509

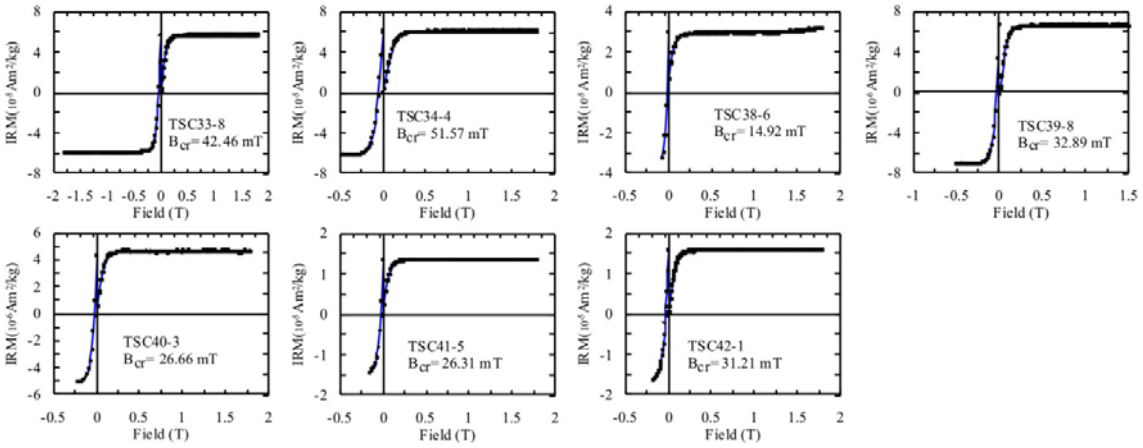

510

511 **Figure DR11:** Isothermal remanent magnetization (IRM) acquisition curves and
512 back-field demagnetization curves for specimens from the Sangri Group volcanics.

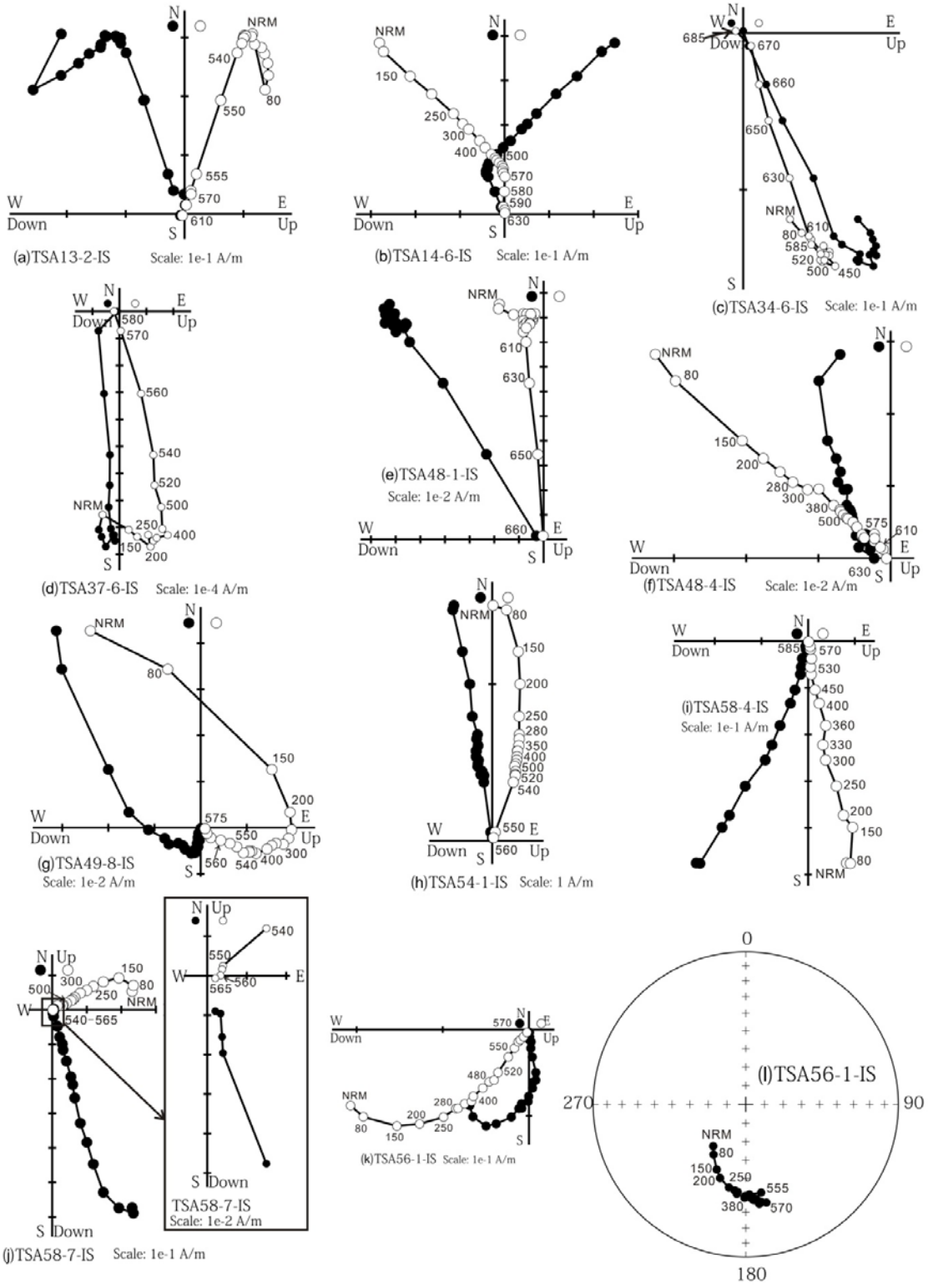
(a)TSA13-2-IS Scale: 1e-1 A/m
(b)TSA14-6-IS Scale: 1e-1 A/m
(c)TSA34-6-IS Scale: 1e-1 A/m
(d)TSA37-6-IS Scale: 1e-4 A/m
(e)TSA48-1-IS Scale: 1e-2 A/m
(f)TSA48-4-IS Scale: 1e-2 A/m
(g)TSA49-8-IS Scale: 1e-2 A/m
(h)TSA54-1-IS Scale: 1 A/m
(i)TSA58-4-IS Scale: 1e-1 A/m
(j)TSA58-7-IS Scale: 1e-1 A/m
TSA58-7-IS Scale: 1e-2 A/m
(k)TSA56-1-IS Scale: 1e-1 A/m
(l)TSA56-1-IS
N
S
W
E
Up
Down
NRM
0
90
180
270

513

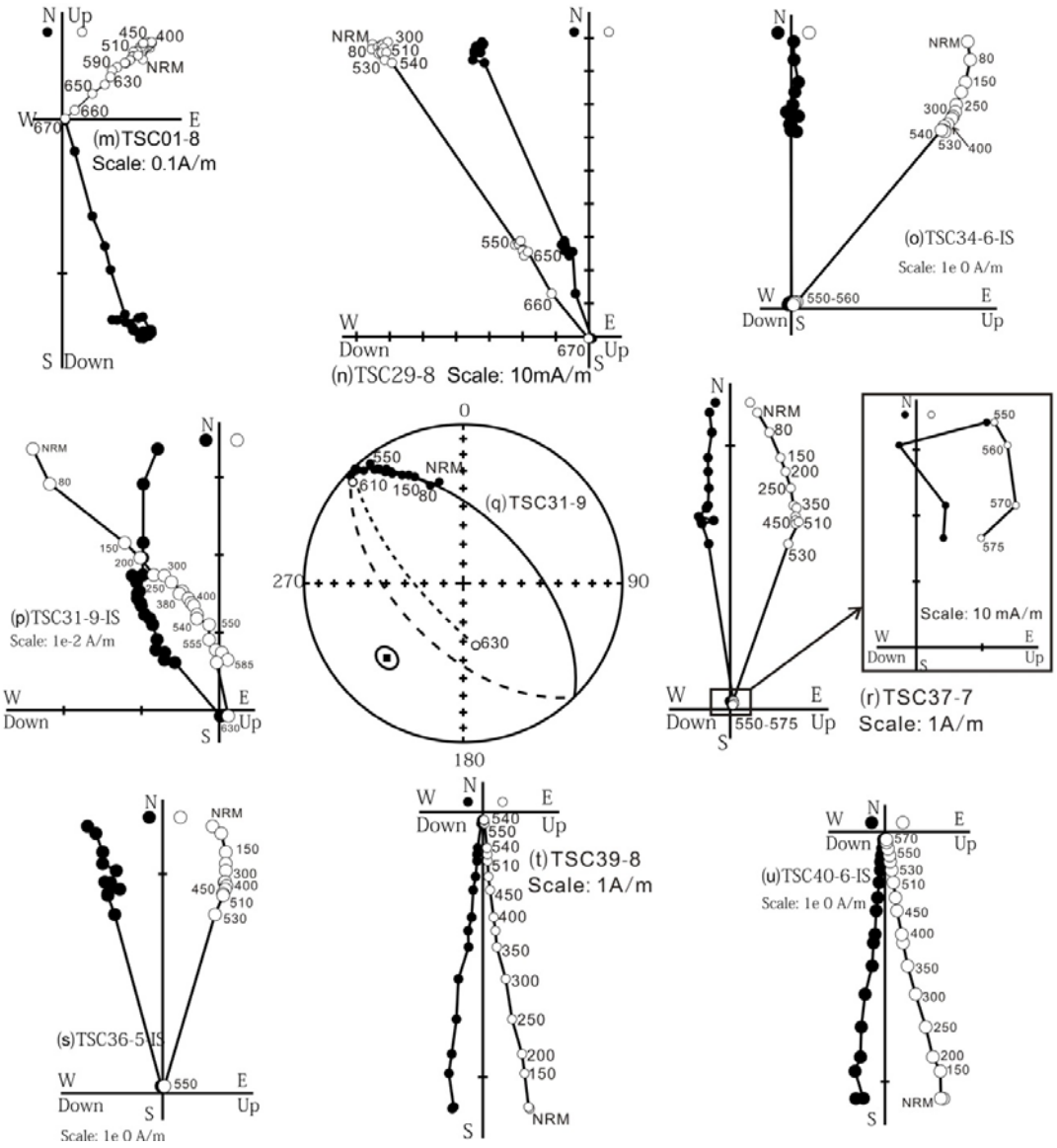

Figure DR12. Step-wise thermal demagnetization results for representative specimens plotted on orthogonal (Zijderveld plot) vector plots and stereonets. All directions are plotted in geographic coordinates; solid (open) circles represent vector endpoints projected onto horizontal (vertical) planes for the vector plots or onto the lower (upper) hemisphere for stereonets. NRM: natural remanent magnetization.

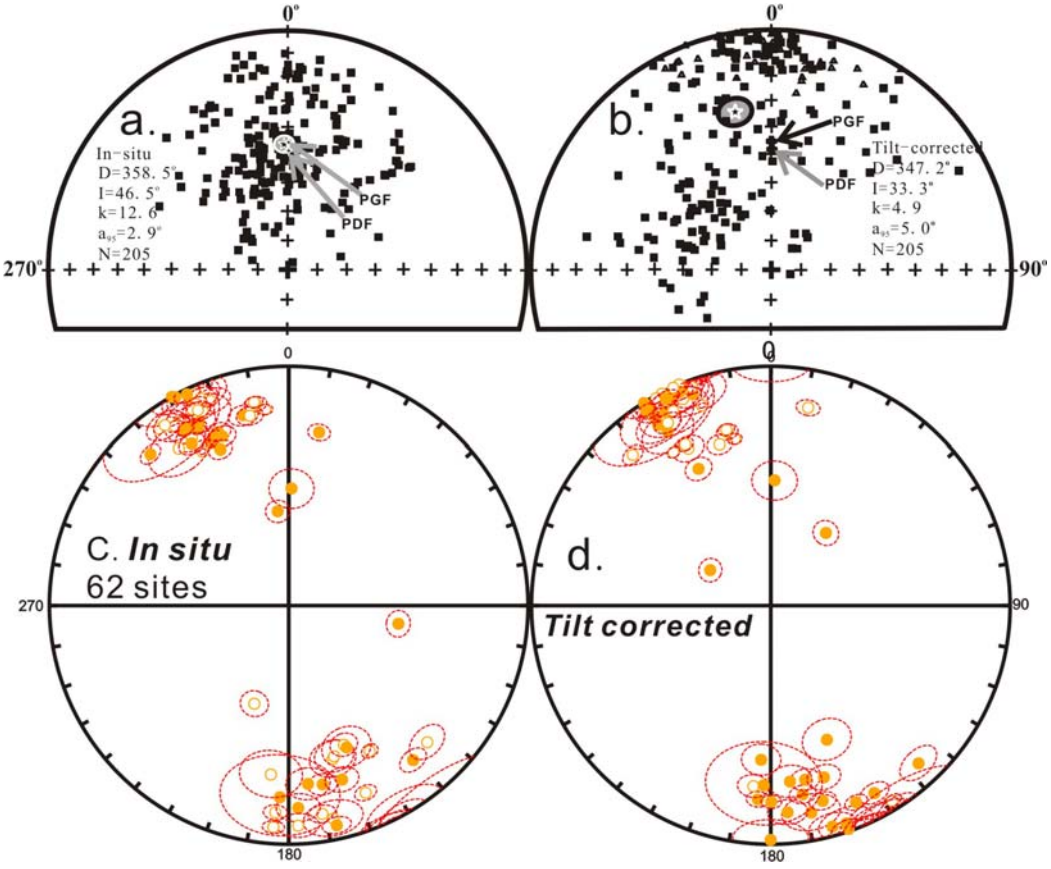

521

522 **Figure DR13:** Stereoplots of magnetic component directions. Component A in *in situ* (a)
523 and tilt corrected (b) coordinates. The mean direction in *in situ* coordinates plots near
524 the present geomagnetic field (PGF) and present dipole field (PDF), suggesting that the
525 component, isolated at low temperatures, records of recent viscous overprint.
526 Component B in *in situ* (c) and tilt corrected (d) coordinates. Directions are antipodal
527 and the best estimate of Fisher's precision parameter (K) improves with structural
528 correction. Upward-pointing (downward-pointing) directions are show by open (closed)
529 circles.

Table DR1.U-Pb Isotopic compositions and corrected ages from the volcanic andesites of the Sangri Group (Samples 2011TS06-7 and 2011TS06-11).

Analysis	CORRECTED RATIOS										CORRECTED AGES (Ma)								Ages (Ma)	1σ
	$^{207}Pb/^{206}Pb$	1σ	$^{207}Pb/^{235}U$	1σ	$^{206}Pb/^{238}U$	1σ	$^{208}Pb/^{232}Th$	1σ	$^{238}U/^{232}Th$	1σ	$^{207}Pb/^{206}Pb$	1σ	$^{207}Pb/^{235}U$	1σ	$^{206}Pb/^{238}U$	1σ	$^{208}Pb/^{232}Th$	1σ		
Sample: 2011TS06-7																				
11TS06-7-01	0.05333	0.03242	0.19892	0.12058	0.02706	0.00127	0.00898	0.00093	1.06	0.01	343	1014	184	102	172	8	181	19	172	8
11TS06-7-02	0.04692	0.04678	0.17636	0.17481	0.02728	0.00299	0.01251	0.00319	2.17	0.02	45	1147	165	151	174	19	251	64	174	19
11TS06-7-03	0.05144	0.03276	0.195	0.12378	0.0275	0.00148	0.00958	0.00131	1.15	0.01	261	999	181	105	175	9	193	26	175	9
11TS06-7-04	0.0492	0.03032	0.18884	0.11567	0.02784	0.00197	0.00923	0.00098	0.77	0.01	157	953	176	99	177	12	186	20	177	12
11TS06-7-05	0.04926	0.01727	0.19263	0.06677	0.02838	0.00156	0.00677	0.00062	0.74	0.01	160	504	179	57	180	10	136	12	180	10
11TS06-7-06	0.04605	0.13696	0.18221	0.54017	0.0287	0.00692	0.01302	0.01039	1.02	0.01	1526	3352	170	464	182	43	261	207	182	43
11TS06-7-07	0.04652	0.03212	0.18697	0.12777	0.02915	0.00296	0.00541	0.00169	1.27	0.01	25	977	174	109	185	19	109	34	185	19
11TS06-7-08	0.05126	0.03712	0.20527	0.14711	0.02905	0.00311	0.00779	0.00131	0.72	0.01	253	1027	190	124	185	19	157	26	185	19
11TS06-7-09	0.04587	0.02871	0.18544	0.11507	0.02933	0.00244	0.00935	0.00164	1.31	0.01	-9	930	173	99	186	15	188	33	186	15
11TS06-7-10	0.05401	0.03461	0.2187	0.13882	0.02938	0.00266	0.01038	0.00157	1.1	0.01	371	1020	201	116	187	17	209	31	187	17
11TS06-7-11	0.05643	0.02379	0.22936	0.09515	0.02949	0.00229	0.00922	0.00114	0.86	0.01	469	653	210	79	187	14	186	23	187	14
11TS06-7-12	0.05177	0.04369	0.21033	0.17608	0.02947	0.00322	0.01331	0.00222	1.04	0.01	275	1168	194	148	187	20	267	44	187	20
11TS06-7-13	0.05373	0.03213	0.23247	0.13788	0.0314	0.00247	0.00912	0.00091	0.52	0.01	360	968	212	114	199	15	184	18	199	15

Analysis	CORRECTED RATIOS										CORRECTED AGES (Ma)								Ages (Ma)	1σ
	$^{207}Pb/^{206}Pb$	1σ	$^{207}Pb/^{235}U$	1σ	$^{206}Pb/^{238}U$	1σ	$^{208}Pb/^{232}Th$	1σ	$^{238}U/^{232}Th$	1σ	$^{207}Pb/^{206}Pb$	1σ	$^{207}Pb/^{235}U$	1σ	$^{206}Pb/^{238}U$	1σ	$^{208}Pb/^{232}Th$	1σ		
Sample: 2011TS06-11																				
11TS06-11-01	0.0502	0.01302	0.17648	0.04521	0.02541	0.0011	0.00952	0.00073	1.11	0.01	204	393	165	39	162	7	192	15	162	7
11TS06-11-02	0.05008	0.0046	0.18051	0.01631	0.02605	0.00044	0.00733	0.00021	0.71	0.01	199	172	168	14	166	3	148	4	166	3
11TS06-11-03	0.04979	0.0184	0.18009	0.06595	0.02625	0.00138	0.00924	0.00082	0.86	0.01	185	547	168	57	167	9	186	16	167	9
11TS06-11-04	0.05478	0.02162	0.20427	0.08038	0.02702	0.00083	0.00912	0.00078	1.21	0.01	403	669	189	68	172	5	184	16	172	5
11TS06-11-05	0.04953	0.00539	0.18889	0.02036	0.02762	0.00041	0.01012	0.00042	2.02	0.02	173	215	176	17	176	3	204	8	176	3
11TS06-11-06	0.05501	0.00445	0.21108	0.0167	0.02787	0.0005	0.00755	0.00024	0.87	0.01	413	146	194	14	177	3	152	5	177	3
11TS06-11-07	0.05522	0.00374	0.21124	0.01391	0.02778	0.00045	0.0071	0.00023	1.1	0.01	421	119	195	12	177	3	143	5	177	3
11TS06-11-08	0.05201	0.00331	0.20182	0.01255	0.0282	0.0004	0.00848	0.00018	0.6	0.01	286	117	187	11	179	3	171	4	179	3
11TS06-11-09	0.0567	0.01214	0.22177	0.04683	0.02839	0.00108	0.0096	0.00067	1.1	0.01	480	377	203	39	180	7	193	13	180	7
11TS06-11-10	0.05125	0.01212	0.20382	0.04801	0.02878	0.00066	0.00725	0.00047	0.92	0.01	252	402	188	40	183	4	146	9	183	4
11TS06-11-11	0.04683	0.0285	0.1865	0.11257	0.02882	0.00249	0.01127	0.00219	1.62	0.02	41	898	174	96	183	16	227	44	183	16
11TS06-11-12	0.04714	0.04925	0.18932	0.19681	0.02909	0.00321	0.01226	0.00273	1.07	0.01	56	1204	176	168	185	20	246	55	185	20
11TS06-11-13	0.05137	0.014	0.21158	0.05719	0.02992	0.0011	0.00953	0.00077	1.17	0.01	257	433	195	48	190	7	192	15	190	7
11TS06-11-14	0.04911	0.01666	0.20507	0.06864	0.03034	0.0018	0.00592	0.00126	1.42	0.01	153	482	189	58	193	11	119	25	193	11
11TS06-11-15	0.05634	0.00978	0.23518	0.03993	0.03033	0.00118	0.0132	0.00161	4.32	0.04	466	306	214	33	193	7	265	32	193	7
11TS06-11-16	0.04912	0.01876	0.20861	0.07874	0.0307	0.00195	0.00889	0.00102	1.06	0.01	154	546	192	66	195	12	179	20	195	12
11TS06-11-17	0.04605	0.01464	0.19664	0.06198	0.03097	0.00131	0.01179	0.00194	0.83	0.01	429	513	182	53	197	8	237	39	197	8
11TS06-11-18	0.05282	0.01406	0.23209	0.06137	0.03181	0.00105	0.00981	0.00067	0.9	0.01	321	440	212	51	202	7	197	13	202	7
11TS06-11-19	0.04779	0.03186	0.20971	0.13869	0.03188	0.00289	0.01509	0.00212	0.99	0.01	89	966	193	116	202	18	303	42	202	18
11TS06-11-20	0.04934	0.01368	0.21825	0.06035	0.03203	0.00068	0.01323	0.00069	1.73	0.02	164	449	200	50	203	4	266	14	203	4
11TS06-11-21	0.05295	0.00914	0.23436	0.03987	0.03214	0.00101	0.00875	0.00042	0.61	0.01	327	312	214	33	204	6	176	8	204	6
11TS06-11-22	0.05349	0.01096	0.23703	0.04777	0.03215	0.0013	0.00766	0.00048	0.58	0.01	350	344	216	39	204	8	154	10	204	8
11TS06-11-23	0.05249	0.00805	0.23442	0.03567	0.03244	0.00067	0.01172	0.00057	1.31	0.01	307	300	214	29	206	4	236	11	206	4
11TS06-11-24	0.05212	0.00885	0.2356	0.03965	0.03281	0.0008	0.01134	0.0006	1.19	0.01	291	315	215	33	208	5	228	12	208	5
11TS06-11-25	0.04943	0.03402	0.22663	0.15495	0.03317	0.00281	0.01082	0.00154	0.71	0.01	168	1000	207	128	210	18	218	31	210	18
11TS06-11-26	0.0534	0.01928	0.24754	0.08874	0.03364	0.00157	0.01078	0.00101	0.84	0.01	346	575	225	72	213	10	217	20	213	10

Table DR2. Information related to thin sections which were used to carry out optical petrography and SEM.

Thin Sections No.	Corresponding Driling Site	Location
11TS26-12	TSa15	Sangri County
11TS26-13	TSa39	Sangri County
11TS26-19	TSa43	Sangri County
11TS27-14	TSa46	Sangye Town
11TS27-22	TSa53	Sangye Town
11TS27-32	TSa60	Sangye Town

Table DR3.1 Summary of hysteresis parameters measured for the Sangri Group volcanic samples (for TSa samples).

Sample ID	Bc (mT)	Mrs (miu Am2)	Ms (miu Am2)	Bcr (mT)	Mrs/Ms	Bcr/Bc	Notes
TSa01-10	22.35	0.125	1.713	54.43	0.072971395	2.435346756	
TSa02-2	18.25	0.05065	1.671	47.32	0.030311191	2.592876712	
TSa03-9	15.59	0.05068	1.466	33.37	0.034570259	2.140474663	
TSa04-1	10.17	0.3767	4.138	27.21	0.091034316	2.675516224	
TSa05-2	18.31	0.0838	1.68	41.91	0.049880952	2.288913162	
TSa06-8	31.54	5.305	13.48	44.51	0.393545994	1.411223843	**FORC**
TSa07-8	13.67	0.0728	1.473	43.18	0.049422946	3.15874177	
TSa08-4	15.45	0.3202	2.961	36.76	0.108139142	2.379288026	
TSa09-6	18.95	0.665	3.613	42.71	0.18405757	2.253825858	
TSa10-4	2.315	0.01704	1.954	42.02	0.008720573	18.1511879	
TSa11-6	6.001	0.01372	1.774	30.1	0.007733935	5.015830695	
TSa12-2	11.38	0.2379	3.78	32.83	0.062936508	2.884885764	
TSa13-7	6.075	8.89	196.8	31.74	0.045172764	5.224691358	
TSa14-6	5.178	3.687	95.5	28.54	0.03860733	5.51178061	
TSa15-5	6.842	2.031	42.56	41.3	0.047720865	6.036246711	**FORC**
TSa16-8	14.61	0.6533	8.44	50.4	0.077405213	3.449691992	**FORC**
TSa17-8	8.854	0.8308	13.43	43.62	0.061861504	4.926586853	
TSa18-2	35.64	0.6442	3.927	77.24	0.164043799	2.167227834	
TSa33-5	40.93	0.9386	3.748	79.71	0.250426894	1.947471292	
TSa34-6	6.882	4.763	101	42.41	0.047158416	6.162452775	**FORC**
TSa35-6	45.49	0.02734	0.6296	209.4	0.043424396	4.603209497	
TSa36-6	8.05	0.09251	2.214	21.79	0.041784101	2.706832298	
TSa37-6	8.684	0.04954	1.184	54.43	0.041841216	6.267848918	
TSa38-8	17.71	7.863	66.44	57.94	0.118347381	3.271597967	
TSa39-6	3.973	6.732	270	33.11	0.024933333	8.333752832	
TSa40-2	4.338	14.61	485.4	25.55	0.030098888	5.889810973	
TSa41-5	7.899	0.0533	1.169	37.71	0.045594525	4.774022028	
TSa42-1	99.8	0.8448	2.245	334.6	0.376302895	3.352705411	
TSa43-1	48.75	1.105	3.895	241.8	0.283697047	4.96	
TSa44-6	78.12	1.099	3.181	301.6	0.34548884	3.860727087	
TSa45-9	4.015	0.01885	1.77	32.8	0.010649718	8.169364882	
TSa46-5	20.47	0.8054	5.149	168	0.156418722	8.207132389	
TSa48-4	18.43	6.527	48.07	63.39	0.135781152	3.439500814	

TSa49-8	9.752	5.886	79.12	38.74	0.074393327	3.972518458	**FORC**
TSa50-6	7.091	31.43	530	30.57	0.059301887	4.311098576	
TSa51-8	14.67	73.57	750.8	50.5	0.097988812	3.442399455	
TSa52-1	10.65	18.94	253.4	44.9	0.074743489	4.215962441	
TSa53-7	4.128	27.46	919.9	26.3	0.029851071	6.371124031	**FORC**
TSa54-1	5.302	37.48	977.2	28.96	0.038354482	5.462089777	
TSa55-1	34.48	18.72	79.17	81.84	0.236453202	2.373549884	
TSa56-1	6.213	5.117	111.6	30.56	0.045851254	4.918718815	
TSa57-4	3.595	10.86	408.1	23.46	0.026611125	6.525730181	
TSa58-7	6.968	15.76	326	35.58	0.048343558	5.10619977	
TSa59-10	5.886	7.031	166.1	29.58	0.042329922	5.0254842	
TSa60-5	9.315	0.8624	22.96	50.19	0.037560976	5.388083736	
TSa61-1	35.44	0.0905	2.066	84.47	0.043804453	2.383465011	
TSa62-4	12.81	0.07116	1.578	89.31	0.045095057	6.971896956	
TSa63-2	18.38	3.559	18.99	46.61	0.187414429	2.535908596	
TSa64-5	22.86	0.5246	2.818	47.75	0.186160397	2.0888014	
TSa65-2	33.04	0.5155	3.467	77.06	0.148687626	2.332324455	
TSa66-9	3.931	0.04368	1.907	51.37	0.022905087	13.06792165	
TSa67-7	19.85	19.63	133.4	51.73	0.147151424	2.60604534	

Table DR3.2 Summary of hysteresis parameters measured for the Sangri Group volcanic samples (for TSC samples).

Sample ID	Bc (mT)	Mrs (miu Am2)	Ms (miu Am2)	Bcr (mT)	Mrs/Ms	Bcr/Bc	Notes
TSC01-8	38.18	1.154	4.422	69.18	0.260967888	1.811943426	**FORC**
TSC04-5	6.507	0.05123	0.9974	110.7	0.051363545	17.01244813	
TSC08-2	7.535	0.07471	1.936	26.4	0.038589876	3.503649635	
TSC09-7	13.14	0.2253	2.445	43.78	0.092147239	3.331811263	
TSC10-3	5.246	0.1119	3.258	23.11	0.034346225	4.405261151	
TSC11-2	4.669	10.37	275.1	25.49	0.037695383	5.459413151	
TSC14-2	1.468	8.604	571.9	8.041	0.015044588	5.477520436	
TSC17-5	2.628	11.34	573.6	15.83	0.019769874	6.023592085	
TSC18-2	5.015	0.5536	13.55	21.99	0.040856089	4.384845464	
TSC19-6	7.353	0.3028	5.942	31.61	0.050959273	4.298925609	
TSC20-4	2.826	0.2411	6.947	12.7	0.034705628	4.49398443	
TSC21-5	18.61	0.09542	1.832	36.86	0.052085153	1.980655562	
TSC22-3	75.27	0.7932	2.296	353.4	0.345470383	4.695097648	
TSC23-5	56.1	0.8661	2.908	345.5	0.297833563	6.158645276	
TSC24-4	44.09	1.39	5.046	244.3	0.275465715	5.540938988	
TSC25-6	45.06	0.9129	3.847	223.7	0.237301794	4.964491789	
TSC26-3	17.71	0.691	4.793	184.3	0.144168579	10.40654997	
TSC28-6	28.15	1.499	7.49	265.9	0.200133511	9.445825933	**FORC**
TSC29-8	7.714	0.7096	10.43	64.53	0.068034516	8.365309826	
TSC30-5	24.81	13.37	81.29	72.72	0.164472875	2.931076179	
TSC31-2	33.01	6.047	29.05	71.27	0.208158348	2.159042714	
TSC32-6	20.15	6.847	45.89	60.85	0.14920462	3.019851117	
TSC33-8	11.9	57.25	704	42.46	0.081321023	3.568067227	
TSC34-4	16.58	62	552.3	51.57	0.112257831	3.110373945	
TSC38-6	4.423	39.24	835.9	14.92	0.046943414	3.373276057	
TSC39-8	6.867	6.565	121	32.89	0.054256198	4.789573322	**FORC**
TSC40-3	7.412	5.377	79.9	26.66	0.067296621	3.596869941	
TSC41-5	5.892	14.47	315.4	26.31	0.04587825	4.465376782	**FORC**
TSC42-1	6.397	16.51	359	31.21	0.045988858	4.878849461	

Table DR4.1 Summary of GPS location of paleomagnetic drilling sites, statistical fisherian mean for ChRMs from the Sangri Group volcanic rocks (for samples labelled with TSa).

Site ID	Sampling Location		Strike/Dip (°)	n0 (N0)	ns(Ns)	n (After 45° cutoff)(N)	In situ		Tilt Corrected		k	α95(°)	Used in Mean (K>50)?
	λs (°)	Φs (°)					Dg(°)	Ig(°)	Ds(°)	Is(°)			
For TSa samples													
Sangri County Location													
TSa05	29.2915	92.0443	271/34	7	7	7	170.9	-12.6	170.4	20.9	256.4	3.8	YES
TSa06	29.2916	92.0441	141/30	5	5	5	334.1	-13.9	339.1	-5.6	67.1	9.4	YES
TSa07	29.2915	92.0442	141/30	4	3	3	323.7	-9.2	328.0	-6.6	53.0	17.1	YES
TSa08	29.2914	92.0441	131/28	4	3	3	330.7	0.1	328.5	9.2	141.5	10.4	YES
TSa09	29.3152	92.0475	131/28	4	3	3	329.4	-11.3	332.4	-1.6	282.0	7.4	YES
TSa10	29.2913	92.0443	129/31	4	4	4	331.4	1.0	328.0	12.2	204.4	6.4	YES
TSa11	29.2913	92.0443	129/31	6	6	6	334.7	4.3	329.3	16.7	77.8	7.6	YES
TSa12	29.2913	92.0443	129/31	5	4	4	347.2	18.5	333.5	35.1	*46.5*	13.6	NO
TSa14	29.2902	92.0451	136/37	5	5	5	141.2	18.1	151.1	11.3	342.4	4.1	YES
TSa15	29.2901	92.0461	130/32	4	4	4	339.1	-9.4	339.8	6.7	297.8	5.3	YES
TSa16	29.2901	92.0461	140/40	5	3	3	336.4	-4.2	336.4	-4.2	247.9	7.8	YES
TSa17	29.2901	92.0462	143/32	5	4	4	336.9	-6.6	338.3	1.7	407.7	4.6	YES
TSa33	29.3126	92.0486	240/40	7	6	6	99.4	51.7	37.1	58.7	246.3	4.3	YES
TSa34	29.3128	92.0486	206/36	9	8	8	168.2	-9.7	168.9	12.7	50.8	7.8	YES
TSa36	29.3133	92.0482	236/39	8	7	7	164.0	-33.6	160.9	3.9	75.1	7.0	YES
TSa37	29.3136	92.0481	271/34	9	9	9	183.7	-14.2	183.8	19.8	257.8	3.2	YES
TSa38	29.3136	92.0479	275/38	9	8	8	175.4	-41.8	177.9	-4.1	*39.0*	9.0	NO
TSa39	29.3139	92.048	253/33	9	6	6	199.3	-54.1	185.5	-25.0	217.2	4.6	YES
TSa40	29.3143	92.048	259/51	7	7	7	166.3	-37.1	166.8	13.8	*44.4*	9.2	NO
TSa41	29.3143	92.048	237/23	6	6	6	177.3	16.2	187.8	2.5	127.9	5.9	YES
TSa42	29.2521	91.9964	220/21.5	9	9	9	337.8	22.9	183.6	35.5	189.2	3.8	YES

Site ID	Sampling Location		Strike/Dip (°)	n0 (N0)	ns(Ns)	n (After 45° cutoff)(N)	In situ		Tilt Corrected		k	α95(°)	Used in Mean (K≥50)?
	λs (°)	Φs (°)					Dg(°)	Ig(°)	Ds(°)	Is(°)			
Sangye Town Location(Northern Bank of the IYZSZ)													
TSa43	29.2521	91.9962	263/45	8	7	7	333.9	15.8	335.5	3.7	161.7	4.8	YES
TSa44	29.2521	91.9962	190/18	9	9	9	331.2	16.6	184.8	-30.0	282.5	3.1	YES
TSa45	29.2521	91.9962	192/20	6	5	5	344.0	28.5	332.3	-26.7	11.6	23.5	NO
TSa46	29.2521	91.9962	222/28	8	5	5	151.0	-30.9	347.8	-29.5	894.0	2.6	YES
TSa47	29.2589	91.9913	260/48	8	7	7	157.0	-42.1	165.1	16.4	34.3	10.5	NO
TSa48	29.2589	91.9913	268/40	8	7	7	134.7	-19.7	161.8	30.4	112.3	5.7	YES
TSa49	29.421	91.8631	260/39	8	8	8	163.3	-34.4	173.7	12.2	86.8	6.0	YES
TSa50	29.421	91.8631	260/39	7	7	7	158.4	-37.4	131.0	31.0	200.7	4.3	YES
TSa51	29.2665	91.7265	290/45	8	5	5	183.7	-41.3	168.9	26.5	28.5	14.6	NO
TSa52	29.2967	91.6237	308/16	7	7	7	177.7	-42.8	162.8	25.7	17.7	14.7	NO
TSa53	29.3001	91.5707	308/16	7	7	7	353.1	-18.7	328.5	4.9	803.5	2.1	YES
TSa54	29.3001	91.5707	308/16	7	6	6	167.7	6.5	173.8	26.7	322.9	3.7	YES
TSa56	29.3392	91.083	313/40	8	8	7	178.7	1.3	178.2	31.8	5.7	27.8	NO
TSa58	29.3393	91.0828	329/47	6	4	4	175.0	-8.9	336.7	17.9	30.8	16.8	NO
TSa60	29.3393	91.0828	324/51	8	8	8	162.4	28.3	1.7	46.4	46.0	8.3	NO
TSa61	29.332	91.0329	285/2	8	8	8	169.3	24.7	148.2	-4.2	168.4	4.3	YES
TSa62	29.332	91.0329	277/1	7	6	6	163.0	24.7	160.4	5.1	187.2	4.9	YES
TSa63	29.333	90.9676	276/1	8	8	8	173.9	25.8	182.3	25.6	76.3	6.4	YES
TSa64	29.333	90.9676	277/2	6	6	6	178.3	29.8	157.4	39.0	37.9	11.0	NO
TSa65	29.333	90.9676	283/5	4	4	3	182.6	20.7	136.9	10.5	55.1	16.8	YES
TSa66	29.333	90.9676	260/3	9	9	8	157.8	36.0	164.4	4.4	53.4	7.7	YES
TSa67	29.333	90.9676	278/3	9	9	8	1.4	49.4	160.8	1.1	60.9	7.2	YES

Table DR4.2 Summary of GPS location of paleomagnetic drilling sites, statistical fisherian mean for ChRMs from the Sangri Group volcanic rocks (for samples labelled with TSC).

Site ID	Sampling Location		Strike/Dip (°)	n0 (N0)	ns(Ns)	After 45° cutoff)	In situ		Tilt Corrected		k	α95(°)	Used in Mean (k>50)?
	λs (°)	Φs (°)					Dg(°)	Ig(°)	Ds(°)	Is(°)			
For TSC samples													
Sangri County Location													
TSC01	29.3128	92.0485	206/36	8	8	8	157.7	-16.3	156.6	11.2	317.8	3.1	YES
TSC02	29.3133	92.0481	236/37	8	6	6	148.9	-41.9	148.2	-4.9	33.8	11.7	NO
TSC04	29.3134	92.0482	236/39	8	4	4	186.0	-29.6	180.0	2.1	100.0	9.2	YES
TSC06	29.2915	92.0443	131/28	8	8	8	4.6	-18.1	6.5	4.9	22.5	11.9	NO
TSC07	29.2915	92.0443	131/28	8	8	8	353.3	57.3	300.4	66.1	198.4	3.9	YES
TSC08	29.2915	92.0442	141/30	8	8	8	336.1	-12.3	340.1	-3.3	295.9	3.2	YES
TSC09	29.2916	92.0441	141/30	8	7	7	334.3	2.3	331.4	8.6	315.1	3.4	YES
TSC10	29.2916	92.0441	141/30	9	9	9	335.3	-8.2	337.5	0.0	320.8	2.9	YES
TSC11	29.2916	92.0441	129/31	8	8	8	329.4	-12.5	332.8	-0.6	483.1	2.5	YES
TSC12	29.2916	92.0441	129/31	7	7	7	327.6	-12.2	331.1	-1.2	777.2	2.2	YES
TSC13	29.2916	92.0441	129/31	8	8	8	333.8	-9.5	335.2	4.1	439.1	2.6	YES
TSC14	29.2916	92.0441	129/31	8	8	8	330.8	-27.0	341.0	-12.7	3060.5	1.0	YES
TSC15	29.2916	92.0441	129/31	7	7	7	330.0	-20.1	337.0	-7.0	148.1	5.0	YES
TSC16	29.2916	92.0441	129/31	7	7	7	335.1	-11.0	336.9	3.4	294.6	3.5	YES
TSC17	29.2911	92.0441	129/31	5	5	5	325.1	-21.0	333.4	-10.0	64.7	9.6	YES
TSC18	29.2911	92.0441	129/31	8	7	7	346.5	19.4	332.2	35.5	208.6	4.2	YES
TSC21	29.2913	92.0443	129/31	8	8	8	325.5	-9.5	328.0	0.2	107.2	5.4	YES

Site ID	Sampling Location		Strike/Dip (°)	n0 (N0)	ns(Ns)	After 45° cutoff)	In situ		Tilt Corrected		k	α95(°)	Used in Mean (k>50)?
	λs (°)	Φs (°)					Dg(°)	Ig(°)	Ds(°)	Is(°)			
Sangye Town Location(Northern Bank of the IYZSZ)													
TSC22	29.2521	91.9964	220/21.5	8	8	8	334.8	25.7	333.4	-2.9	1015.5	1.7	YES
TSC23	29.2521	91.9964	220/21.5	8	8	8	336.6	23.6	334.3	4.2	819.3	1.9	YES
TSC24	29.2521	91.9962	263/45	7	7	7	333.1	17.8	332.1	-24.7	606.5	2.5	YES
TSC25	29.2521	91.9962	263/45	9	9	9	329.2	16.3	327.7	-25.0	687.6	2.0	YES
TSC26	29.2521	91.9962	190/18	8	8	8	329.7	15.6	327.4	3.6	490.3	2.5	YES
TSC28	29.2527	91.9958	222/28	8	8	8	338.6	25.0	335.9	-0.4	191.5	4.0	YES
TSC29	29.2527	91.9958	222/28	8	8	8	336.4	29.5	333.1	3.6	244.0	3.6	YES
TSC30	29.259	91.9913	268/40	8	8	8	317.6	15.4	317.6	-15.6	299.2	3.2	YES
TSC31	29.259	91.9913	268/40	13	13	13	329.1	22.1	330.6	-13.4	114.3	3.9	YES
TSC34	29.2665	91.7263	290/45	8	8	8	10.0	27.4	10.7	-17.0	285.9	3.3	YES
TSC35	29.2665	91.7263	290/45	8	7	7	16.0	20.4	15.8	-24.5	29.2	11.4	NO
TSC36	29.3001	91.5706	308/16	9	9	9	350.6	-15.8	345.9	-26.1	273.5	3.1	YES
TSC37	29.3001	91.5706	308/16	6	6	6	348.4	-20.2	342.4	-30.0	314.0	3.8	YES
TSC38	29.3001	91.5707	308/16	8	8	8	350.3	-14.9	345.8	-25.3	554.6	2.4	YES
TSC39	29.3393	91.0827	329/47	8	8	8	177.5	-8.5	175.4	14.2	108.0	5.4	YES
TSC40	29.3393	91.0827	329/47	8	8	8	184.0	-7.7	179.8	18.9	382.1	2.8	YES
Overall mean for selected sites							**336.2**	**5.2**			**12.6**	**2.5**	
						517			**335.7**	**-4.3**	**18.2**	**2.1**	
				76 (558)	63 (521)	62 (517)							

Abbreviations are as follow: Site ID, Site identification; **λs and Φs**, denote latitude and longitude of the sampling site location; **Strike/dip**, azimuth of right-hand strike and dip angle of the Sangri Gr. Volnic rocks; **n0(N0), ns (Ns), n (After 45° cut-off)/n**, number of samples which were demagnetized; total number of sites/samples within a site before 45° cut-off; number of sites/samples which are used to join calculating fisherian mean after 45° cut-off; **Dg, Ig (Ds, Is)**, declination and inclination of site mean direction before (after) bedding correction; **k**, estimate of precision parameter of Fisher statistics; **α95**, radius of 95% confidence circle about the caculated mean direction.

Table DR5.1 Compiled paleopoles from Chinese and English literatures are used for building continuously varied curves of paleolatitude versus age (Results from the Lhasa block).

	Sampling Location				Paleopole position															
Sampling Location	**λs (°)**	**Φs (°)**	**N (n)**	**Ns (ns)**	**Ds**	**ΔDx**	**Is**	**ΔIx**	**λp (°)**	**Φp (°)**	**K**	**A95**	**A95min**	**A95max**	**Min Palat.**	**Max Palat.**	**Age (Ma)**	**Min Age (Ma)**	**Max Age (Ma)**	**Sources**
Results from Lhasa Block, reference point (29 °N, 88 °E)																				
Gerze	32.2	84.3	35	35	340.1	3.3	42.4	4.0	58.6	324.1	66.4	3.0	2.9	8.7	21.6	27.6	35	30	40	1
Penbo	29	88	52	52	7.1	3.7	36.4	5.1	67.5	17.4	33.5	3.5	2.5	6.8	16.9	23.9	51.5	47	56	2
Nanmulin	29.8	89.2	20	20	339.3	5.1	44.9	5.7	56.6	325.5	51.7	4.6	3.6	12.4	22.1	31.3	52	51.4	52.6	3
Pana Fm, Penbo	30	91.2	119	119	10.5	3.1	44.5	3.5	60.7	18.9	23.1	2.8	1.8	4.0	23.5	29.0	52	51	53	4
Maxiang	29.9	90.7	97	97	343.1	3.3	34.7	4.8	63.6	322.1	21.8	3.1	1.9	4.6	16.1	22.4	83	66	100	5
Penbo 2	29.9	90.7	43	43	350.4	2.6	22.3	4.6	74.7	321.4	73.8	2.6	2.7	7.7	9.1	14.2	97	90	104	6
Deqing and Cuoqin	31.2	84.5	30	30	335.5	5.8	30.9	8.9	60.0	307.6	23.2	5.6	3.1	9.6	11.4	22.7	120	110	130	7, 8
Yahu	32.2	82.8	51	51	28.6	2.3	36.4	3.2	55.2	52.0	84.0	2.2	2.5	6.9	18.1	22.5	126	120	132	9
Sangsang, Xigaze forearc	29.3	86.6	117	117	350.8	4.3	30.4	6.6	69.3	334.8	11.2	4.1	1.8	4.1	12.4	20.7	128	125	131	10
Lhasa	29.7	91.1	17	21	344.0	13.4	11.6	25.8	71.8	290.5	8.1	13.3	3.9	13.8	-7.3	20.9	154	145	164	11
Sangxiong	31.12	91.48	32	32	350.2	5.5	-14.7	10.5	77.4	231.9	22.4	5.5	3.0	9.2	-13.2	-2.1	154	145	164	12
Gainze	32	84	6	6	333.9	15.8	-30.6	24.3	59.6	234.1	20.7	15.1	5.9	26.5	-35.4	-3.1	154	145	164	13
Daxiong	30.5	85	4	4	321.1	14.0	-27.1	22.9	49.0	247.1	46.9	13.6	6.9	34.2	-30.8	-2.1	173	145	201	13
Sangri Group Lavas	29.3	92	61	63	340.1	3.5	-7.7	6.9	70.0	258.4	27.7	3.5	2.3	6.2	-7.5	-0.4	179.9	172.7	187.1	This Study
Dazi, Jiangda	29.44	91.27	13	13	344.7	10.3	-22.9	17.8	69.8	229.0	18.1	10.0	4.3	16.3	-23.2	-2.5	182.5	164	201	12
Dazi Bridge	29.41	91.26	22	22	65.6	5.7	-37.4	7.7	22.6	114.1	35.1	5.3	3.5	11.7	-26.6	-15.9	218	201	235	12
Qusang	30	90.8	19	25	357.0	15.6	-54.9	12.6	48.1	184.5	8.0	12.7	3.7	12.8	-50.4	-24.4	218	201	235	11
Dibucuo north_T3	30.86	84.72	37	37	49.3	5.2	-31.6	7.8	38.0	113.2	23.9	4.9	2.8	8.4	-22.3	-12.4	219	201	237	14
Deqing	29.6	90	12	13	323.7	16.9	-50.9	15.7	41.6	222.1	10.1	14.4	4.4	17.1	-49.2	-19.4	241	235	247	11
Dibucuo north_T1-2	30.86	84.71	47	47	55.9	2.0	-30.3	3.1	32.4	109.8	121.1	1.9	2.6	7.3	-18.2	-14.4	244.5	237	252	14
Xianza, Zhakang	30.9	89.2	16	16	41.9	6.4	-28.0	10.3	45.4	112.8	36.9	6.2	4.0	14.3	-21.5	-9.1	285.5	272	299	15
Xianza and Cuoqin	30.8	84.9	8	9	42.5	17.9	3.5	35.6	47.2	86.2	10.6	17.9	5.2	22.1	-17.5	22.1	285.5	272	299	16
Xianza	30.57	88.43	7	7	357.1	8.9	-35.3	12.5	69.7	188.5	53.0	8.4	5.5	24.1	-28.9	-11.8	285.5	272	299	12
Xianza limestone	30.8	89.3	4	7	285.3	36.1	21.3	63.6	16.3	283.2	7.7	35.3	6.9	34.2	-24.5	79.9	311	299	323	16
Xianza 2	31.01	88.42	28	28	344.2	7.2	-19.4	13.0	70.4	235.7	15.9	7.1	3.2	10.0	-17.6	-3.2	311	323	299	12
Xianza 3	31	88.45	39	45	331.8	9.2	-33.4	13.5	56.0	231.1	7.9	8.7	2.8	8.2	-28.1	-10.3	329	299	359	12, 13

Table DR5.2 Compiled paleopoles from Chinese and English literatures are used for building continuously varied curves of paleolatitude versus age (Result from the Qiangtang block).

	Sampling Location				Paleopole position															
Sampling Location	**λs (°)**	**Φs (°)**	**N (n)**	**Ns (ns)**	**Ds**	**ΔDx**	**Is**	**ΔIx**	**λp (°)**	**Φp (°)**	**K**	**A95**	**A95min**	**A95max**	**Min Palat.**	**Max Palat.**	**Age (Ma)**	**Min Age (Ma)**	**Max Age (Ma)**	**Sources**
Latest result from Qiangtang Block, reference point (29 °N, 88 °E)																				
Jiapila Formation_T3	34.1	92.4	240	210	31.7	2.9	52.0	2.6	44.5	38.8	17.3	2.4	1.4	2.8	30.3	35.1	208.5	203.6	213.3	17

Table DR5.3 Compiled paleopoles from Chinese and English literatures are used for building continuously varied curves of paleolatitude versus age (Results from the Tethys-Himalayan block).

	Sampling Location								Paleopole position										
Sampling Location	**λs (°)**	**Φs (°)**	**N (n)**	**Ns (ns)**	**Ds**	**ΔDx**	**Is**	**ΔIx**	**λp (°)**	**Φp (°)**	**K**	**A95**	**A95min**	**A95max**	**Min Palat.**	**Max Palat.**	**Age (Ma)**	**Min Age (Ma)**	**Max Age (Ma)**	**Sources**
Results from Tethys-Himalayan Block, reference point (29°N, 88°E)																				
TH, Upper Zhongpu	28.3	88.5	14	14	356.6	2.9	18.9	5.2	79.6	341.3	200.8	2.8	4.2	15.6	7.0	12.6	57.5	56	59	18
TH, Lower Zhongpu	28.3	88.5	18	18	0.6	3.2	10.6	6.2	84.5	5.9	120.2	3.2	3.8	13.3	2.2	8.6	60.5	59	62	18
TH - Zongshan	28	89.2	142	144	3.4	3.3	-11.9	6.4	82.3	152.8	13.8	3.3	1.7	3.6	-9.4	-2.8	68	65	71	19, 20
TH - Takkhola	28.8	83.8	95	95	334.1	4.9	-62.0	3.0	39.3	203.2	17.4	3.6	1.9	4.7	-46.9	-39.7	119	113	125	21
TH-Sangxiu Formation_K1	28.8	91.3	26	26	296.9	5.7	-66.6	2.7	16.9	217.2	59.9	3.7	3.3	10.5	-53.0	-45.6	129.75	124.4	135.1	22
TH - Lakang	28.1	92.4	33	35	264.5	9.7	-67.6	4.4	-3.7	218.5	17.7	6.1	3.0	9.1	-57.0	-44.7	132.5	131	134	23
TH, Wolong volcanic sst	28.5	87	198	200	20.2	5.3	-71.2	2.0	30.6	167.1	12.1	3.0	1.4	2.9	-58.8	-52.8	134	130	138	24
TH - Khrew 1	34.06	75.04	24	24	279.3	10.0	-47.0	10.6	7.7	238.3	12.2	8.8	3.4	11.1	-38.2	-20.3	218	201	235	25
TH - Takkhola 2	28.8	83.7	21	22	324.5	11.7	-36.8	16.0	48.8	234.1	9.4	11.0	3.6	12.0	-33.4	-10.7	219	209	228	21
TH - Naubug	33.63	75.39	16	18	272.1	17.1	-52.9	14.8	1.8	232.5	7.7	14.2	4.0	14.3	-50.7	-21.4	226	201	252	25
TH - Manang	28.7	84.1	40	40	333.7	4.9	-52.5	4.4	47.4	212.6	30.9	4.1	2.7	8.0	-37.5	-29.2	228	209	247	26
TH - Shiar 1	28.6	85.1	87	133	11.4	6.4	-63.4	3.6	41.6	169.8	12.4	4.5	2.0	4.9	-49.7	-40.7	228	209	247	27
TH - Takkhola 1	28.8	83.7	35	35	327.2	5.7	-46.8	6.1	47.0	224.0	24.1	5.0	2.9	8.7	-33.4	-23.3	235	228	242	21
TH - W. Doplo	29.4	82.97	67	109	288.1	12.4	-74.6	3.6	7.4	206.1	9.5	5.9	2.2	5.8	-67.4	-55.5	237.5	228	247	28
TH - Khrew 2	34.06	75.04	28	28	278.0	9.6	-52.3	8.5	5.6	234.9	12.5	8.0	3.2	10.0	-41.8	-25.6	242.5	235	247	25
TH - Shiar 2	28.6	85.1	24	27	2.0	6.2	-59.0	4.3	49.1	177.6	39.2	4.8	3.4	11.1	-44.9	-35.3	247	242	252	27
TH - Barsu	33.9	75.02	23	25	277.1	18.9	-71.3	6.8	4.7	211.3	9.4	10.4	3.4	11.4	-67.2	-46.3	249.5	247	252	25
TH - Barsu 2	33.9	75.02	67	83	265.7	8.3	-66.9	3.9	-3.3	218.1	11.4	5.4	2.2	5.8	-55.1	-44.4	251.5	251	252	25
TH - W. Doplo 2	29.3	82.97	10	19	295.4	10.7	-66.3	5.2	16.4	217.9	48.2	7.0	4.8	19.2	-56.3	-42.2	251.5	251	252	28

Notes are as follows: **λs and Φs**, latitude and longitude of the sampling site location; **λp and Φp**, latitude and longitude of the paleopoles published previously and from this study; **A95**, radius of the 95% confidence circle (confidence ellipse)/semi-axis of the ellipse of confidence around the paleopole; **N(n)**, number of sites (samples) used in calculating fisherian mean; **Plat.**, denotes the paleolatitude derived from paleopoles from published literatures and this study at the reference site; **Sources**, cited references in this study, 1, Ding et al., 2014; 2, Lippert. et al., 2014; 3, Huang et al., 2015a; 4, Huang et al., 2013; 5, Sun et al., 2012; 6, Tan et al., 2010; 7, Chen et al., 2012; 8, Yang et al., 2014; 9, Ma et al., 2014; 10, Huang et al., 2015b; 11, Zhu et al., 1985; 12, Dong et al., 1991; 13, Ye and Li, 1987; 14, Zhou et al., 2016; 15, Ran et al., 2012; 16, Guo, 2009; 17, Song et al., 2015; 18, .Yi et al., 2011; 19, Patzelt et al., 1996; 20, Dupont-Nivet et al., 2010; 21, Klootwijk and Bingham, 1980; 22, Ma et al., 2016; 23, Yang et al., 2015; 24, Huang et al., 2015c; 25, Klootwijk et al., 1983; 26, Appel et al., 1991; 27, Schill et al., 2002; 28, Crouzet et al., 2003.